IMA Journal of Applied Mathematics (2020) **85**, 790–821
doi:10.1093/imamat/hxaa021
Advance Access publication on 22 July 2020

Fast and spectrally accurate numerical methods for perforated screens (with applications to Robin boundary conditions)

Matthew J. Colbrook* and Matthew J. Priddin
DAMTP, University of Cambridge
*Corresponding author: m.colbrook@damtp.cam.ac.uk

[Received on 29 August 2019; revised on 10 April 2020; accepted on 24 June 2020]

This paper considers the use of compliant boundary conditions to provide a homogenized model of a finite array of collinear plates, modelling a perforated screen or grating. While the perforated screen formally has a mix of Dirichlet and Neumann boundary conditions, the homogenized model has Robin boundary conditions. Perforated screens form a canonical model in scattering theory, with applications ranging from electromagnetism to aeroacoustics. Interest in perforated media incorporated within larger structures motivates interrogating the appropriateness of homogenized boundary conditions in this case, especially as the homogenized model changes the junction behaviour considered at the extreme edges of the screen. To facilitate effective investigation we consider three numerical methods solving the Helmholtz equation: the unified transform and an iterative Wiener–Hopf approach for the exact problem of a set of collinear rigid plates (the difficult geometry of the problem means that such methods, which converge exponentially, are crucial) and a novel Mathieu function collocation approach to consider a variable compliance applied along the length of a single plate. We detail the relative performance and practical considerations for each method. By comparing solutions obtained using homogenized boundary conditions to the problem of collinear plates, we verify that the constant compliance given in previous theoretical research is appropriate to gain a good estimate of the solution even for a modest number of plates, provided we are sufficiently far into the asymptotic regime. We further investigate tapering the compliance near the extreme endpoints of the screen and find that tapering with tanh functions reduces the error in the approximation of the far field (if we are sufficiently far into the asymptotic regime). We also find that the number of plates and wavenumber has significant effects, even far into the asymptotic regime. These last two points indicate the importance of modelling end effects to achieve highly accurate results.

Keywords: spectral methods; acoustic scattering; perforated screens; Robin boundary conditions.

1. Introduction

The scattering of waves by sets of collinear plates or gratings forms a canonical scattering problem of interest in a range of applications including optics (Sturman *et al.*, 2011), electromagnetism (Chen, 1971; Daniele *et al.*, 1990; Guizal & Felbacq, 1999; Nye, 2002; Otoshi, 1971) and acoustics (Jin *et al.*, 2019). While diffraction gratings exist in a plethora of designs, the most simplistic transmission grating is that consisting of periodically spaced plates as illustrated in Fig. 1. Despite its simplicity, there has been continued interest in the problem since the 1950's (Achenbach & Li, 1986; Erbaş & Abrahams, 2007; Heins & Baldwin, 1954), particularly for acoustic wave scattering. While many acoustic problems for a single finite plate can be solved in closed form with the use of special functions (e.g. via separation of variables in elliptic coordinates), there is no such solution for multiple plates. This limitation has spawned a variety of numerical solution approaches, including several spectrally accurate numerical schemes developed recently in Colbrook *et al.* (2019a); Priddin *et al.* (2020); Llewellyn Smith & Luca (2019).

FIG. 1. A perforated screen with aperture width $2a$ and separation d.

Previous work most commonly considers infinite gratings. However, with recent renewed interest in applications such as the silent flight of owls (Graham, 1934; Jaworski & Peake, 2020, 2013; Lilley, 1998), there have been studies into the effects of noise reduction due to truncated perforated plates (also referred to as porous plates) both experimentally and theoretically (Geyer *et al.*, 2010; Kisil & Ayton, 2018; Priddin *et al.*, 2019). A natural model for such physical designs is a finite grating, but since it is difficult to model the precise setup of a porous plate, the typical approach in these finite grating investigations is to homogenize the boundary condition, finding an effective compliance of the plate and applying this over the whole grating's length. This analysis provides a Robin boundary condition constructed to capture the macroscopic phenomena of interest, allowing a more straightforward analysis of structures involving the perforated material. It is desirable to understand the appropriateness of this approximation to inform the development of physical designs, especially as the precise nature of material junctions is known to be significant in scattering problems, and aerodynamic considerations encourage the use of small porous elements. Throughout this paper we refer to compliance as defined by Leppington (1977), wherein we mean the surface is locally reactive but elastic forces are negligible.

Early work by Lamb (1895) calculated the effective compliance of a two-dimensional infinite grating comprised of thin plates and slits and obtained a constant compliance in this case, dependent on the plate and slit lengths.[1] Rayleigh calculated the conductivity of a circular aperture (Rayleigh, 1896, §307) and thus the effective compliance of an infinite screen perforated with circular holes. This was extended to the case of flow by Howe (1998) (see also Grace *et al.*, 1998, 1999). These works also gave rise to a constant effective compliance that has been used to classify the porosity of plates in recent applications relating to quiet flight (Cavalieri *et al.*, 2014, 2016; Jaworski & Peake, 2013; Kisil & Ayton, 2018). The effective compliance of more complex pore geometries has been recently considered theoretically in Laurens *et al.* (2014), and it may also be determined experimentally by measuring acoustic impedance Dalmont (2001). We emphasize that, for aeroacoustic investigations, such a uniform effective compliance associated with an infinite medium has been repeatedly applied on truncated sections.

However, Leppington's (Leppington, 1977) analysis of the edge effects of semi-infinite perforated screens indicates that the effective compliance ought not to be constant, and the constant approximation holds only in the infinite grating limit. Despite this finding by Leppington, to the best of the authors' knowledge, no one has taken account of this variable compliance when considering acoustic scattering by perforated plates when finite edges are present. Previous studies have considered both scattering by finite diffraction gratings (Guizal & Felbacq, 1999) and explicit consideration of truncation effects on electromagnetic scattering by a semi-infinite array of dipoles (Camacho *et al.*, 2019; Capolino & Albani, 2009), but this is typically isolated from the notion of an effective boundary condition.

This paper, therefore, investigates the effective compliance of finite gratings and the influence of edge effects on the far-field scattered noise due to an incident plane wave. To do so, we employ numerical methods to accurately solve for the scattered field, accounting for the precise grating

[1] For a more recent derivation of homogenized boundary conditions for periodic arrangements of obstacles, see also Hewett & Hewitt (2016).

geometry, and compare to the scattered field when a constant or variable homogenized compliance is imposed. As Leppington's results only provide asymptotic limits for the compliance at the edge and far from the edge, we further investigate the influence on the scattered field as one transitions between these two limits.

The ubiquity of singular integral equations and singular edge behaviour in these problems means care is required in all numerical implementations. While standard boundary element techniques could, in principle, be employed, this would be difficult for the appropriate asymptotic regime considered in this paper. We, therefore, take the opportunity to compare two recently developed approaches based upon a spectral formulation. These two methods, the extension of the unified transform method to scattering problems (Colbrook *et al.*, 2019a) and an iterative Wiener–Hopf method (Priddin *et al.*, 2020), have both individually been seen to be spectrally convergent for acoustic scattering problems consisting of finite flat plates. The unified transform approach can also treat more general geometries. In addition to using these two methods to consider the impact of homogenized boundary conditions on perforated plates and gratings, we also discuss their relative performance for such scattering problems giving indications as to which method is best suited for grating-related problems, particularly as parameters vary; for instance, the number of plates and characteristic Helmholtz numbers associated with the problem. We also seek to note qualitative and practical differences of interest for those wishing to apply or extend our approaches.

Finally, in order to consider variable compliance, this paper presents an accurate (and simple) collocation method, based on Mathieu functions, for solving scattering by a finite plate with a variable Robin boundary condition imposed along the chord. Such a variable Robin condition has been investigated for considering the aerodynamic problem of thin aerofoils with porosity gradients (Baddoo *et al.*, 2014; Hajian & Jaworski, 2017) where the authors solve the Laplace equation. The present Mathieu collocation method may be used to solve the complementary aeroacoustic problem, namely a Helmholtz equation problem, and so we believe it may be of broad interest in this community. Future work will seek to extend this approach to include other boundary conditions, such as those modelling elasticity.

The layout of this paper is as follows. We first describe the mathematical modelling of scattering by a set of collinear plates and review results on the use of homogenized boundary conditions to be interrogated. We then outline the unified transform and iterative Wiener–Hopf method applied to the problem of collinear finite plates, highlighting similarities and divergences between these approaches and compare their performance. To investigate a variable Robin condition imposed on a finite screen, we introduce a separation of variables boundary collocation method (which we believe may be of further interest in the acoustic community). Finally, we compare the use of the homogenized boundary condition to the exact case, indicating the appropriateness of its use in relevant parameter regimes.

2. The mathematical model

In this paper, we are primarily concerned with the scattering of acoustic sources by a finite collection of collinear plates as illustrated in Fig. 2. We denote the set of plates by $\gamma = \cup_{i=1}^{M}\gamma_i$, where each plate is located at $y = 0$ and $x \in [x_{i,0}, x_{i,1}] = \gamma_i$ with $x_{i,0} < x_{i,1} < x_{i+1,0}$ (i.e. the plates do not touch). Thus our total scattering domain consists of $\mathbb{R}^2\backslash\gamma$, where the scattered field q must satisfy the Helmholtz equation

$$\frac{\partial^2 q}{\partial x^2} + \frac{\partial^2 q}{\partial y^2} + k_0^2 q = 0, \tag{2.1}$$

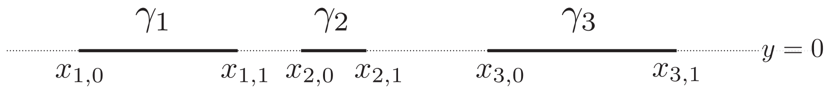

FIG. 2. Example of the geometry and labelling convention for three plates.

for acoustic wavenumber k_0. An example of the set up for three plates with labelled endpoints is shown in Fig. 2.

A canonical heterogeneous obstacle is a perforated screen or grating that is a sound-hard wall with several small open apertures—see Fig. 1. On the sound-hard plates we impose a Neumann boundary condition, and away from the plates a continuity condition, which here is equivalent to a sound-soft boundary:

$$\frac{\partial q}{\partial y}(x,0) + \frac{\partial q_I}{\partial y}(x,0) = 0 \quad x \in \gamma, \quad [q](x,0) := q(x,0_+) - q(x,0_-) = 0 \quad x \in \mathbb{R} \setminus \gamma, \tag{2.2}$$

where q_I denotes the incident field. The typical choice in this paper is

$$q_I(x,y) = \mathrm{e}^{-\mathrm{i}k_0 x \cos\theta - \mathrm{i}k_0 y \sin\theta} \tag{2.3}$$

corresponding to a wave incident at angle θ measured in the anti-clockwise direction from the positive x-axis. Throughout, we will also impose the Sommerfeld radiation condition on the scattered field q.

Rather than solving for each disjoint boundary condition, the screen can be considered to have one homogenized Robin boundary condition in appropriate limits as we now discuss. In scattering problems, the fundamental quantities of interest are typically the far-field wave scattered by an obstacle, or if the obstacle divides two regions, the reflection and transmission coefficients across this border such as that calculated in Lamb (1895). If the obstacle is heterogeneous, but only due to defects that are small relative to all other length scales, then we might naturally seek a homogenized boundary condition that captures the important macroscopic effects on these physically relevant quantities.

If the wavelength $2\pi/k_0$ of the incident disturbance is much larger than the length scales of the grating, i.e. the aperture width $2a$ and spacing d, then the defects are compact, and we observe the desired separation of scales to permit homogenization of the boundary condition. Our focus concerns the use of effective compliance (Leppington, 1977) as this homogenized boundary condition, i.e. approximating the boundary conditions on the plates by a boundary condition on the full screen of the form

$$\frac{\partial q}{\partial y}(x,0) + \frac{\partial q_I}{\partial y}(x,0) = \mu(x)[q](x,0), \quad x \in [x_{1,0}, x_{M,1}] \tag{2.4}$$

in order to model a perforated screen of finite extent. Typically, we will take $[x_{1,0}, x_{M,1}] = [-1,1]$, which is without loss of generality since we can always non-dimensionalize lengths by the semi-chord of the screen. We will refer to this boundary condition as a Robin boundary condition, consistent with the partial differential equation (PDE) literature.

Leppington (1977) considered scattering by a perforated screen of semi-infinite extent ($x \in \mathbb{R}_{\geq 0}$) formed from a set of collinear plates and the homogenized boundary condition this required. By first constructing an integral equation associated with the scattering problem and restricting attention to the asymptotic regime

$$a \ll d \ll k_0^{-1}, \tag{2.5}$$

the effective compliance at $x \gg d$ was found to be

$$\mu = \mu_0 = \frac{\pi}{2d}\left\{\log\left(\frac{d}{\pi a}\right)\right\}^{-1} \tag{2.6}$$

consistent with results in Lamb (1895) for an infinite screen. Leppington also analysed a formula for the effective compliance when $x \sim d$ near the plate edge. However, the analysis breaks down for smaller x, and it is not clear how one should let μ approach zero at the end of the plate. In fact the formula given in Leppington (1977) becomes negative for small enough $x \sim a$. A correction enforcing $\mu \geq 0$ was also proposed, but this leads to $\mu(x) \uparrow \infty$ as $x \downarrow 0$ as opposed to the physically correct value $\mu(0) = 0$.[2] In general, there is very little said in the literature about the values of μ close to the plate ends. For our finite screen, we will therefore consider the constant compliance given by (2.6) as well as different approaches of tapering the effective compliance to zero at both plate edges (see § 6.3).

The numerical methods considered for solving the non-homogenized problem (2.2) in this paper enable the direct interrogation of when these homogenized boundary conditions (2.4) may be appropriate: i.e. how 'deep' within the asymptotic regimes we must be in order for a homogenized boundary condition to offer a good approximation. Three primary limits present themselves:

(a) How small must the open area fraction (i.e. void fraction, or porosity in other subjects) $2a/d$ be?

(b) How small must the grating Helmholtz number $k_0 d$ be?

(c) How large must the screen Helmholtz number $2k_0$ or the number of plates M be for end effects to be negligible?

2.1 *The numerical approaches*

We consider two spectral methods to solve the problem of scattering by a set of collinear finite rigid plates. The differences between the two approaches are illustrated in Fig. 3. Both approaches start with essentially the same equation relating integral transforms of the unknown boundary values (the 'global relation'), though each employs a distinct solution method. The unified transform simply views this equation as providing a set of linear relations parametrized by a variable α (and hence is applicable to more general problems/geometries). This equation may be discretized by choosing a suitable basis for the unknown physical boundary values, and the resulting linear system is solved by collocation, employing closed form expressions for the Fourier transforms of the basis functions. By contrast, the iterative Wiener–Hopf approach views the global relation as defining a jump problem between sectionally analytic functions: a matrix Wiener–Hopf problem that may be solved by considering a sequence of scalar Wiener–Hopf problems to give a fixed-point iteration scheme. For the problem considered in this paper, this iterative process has a physical interpretation as the analogue of Schwarzschild diffraction series (Shanin, 2003) in the spectral domain. Practically, the iterative Wiener–Hopf method requires choosing a basis for the jumps of functions along branch cuts and employing

[2] For a porous plate, a hole cannot exist at the end point of the plate.

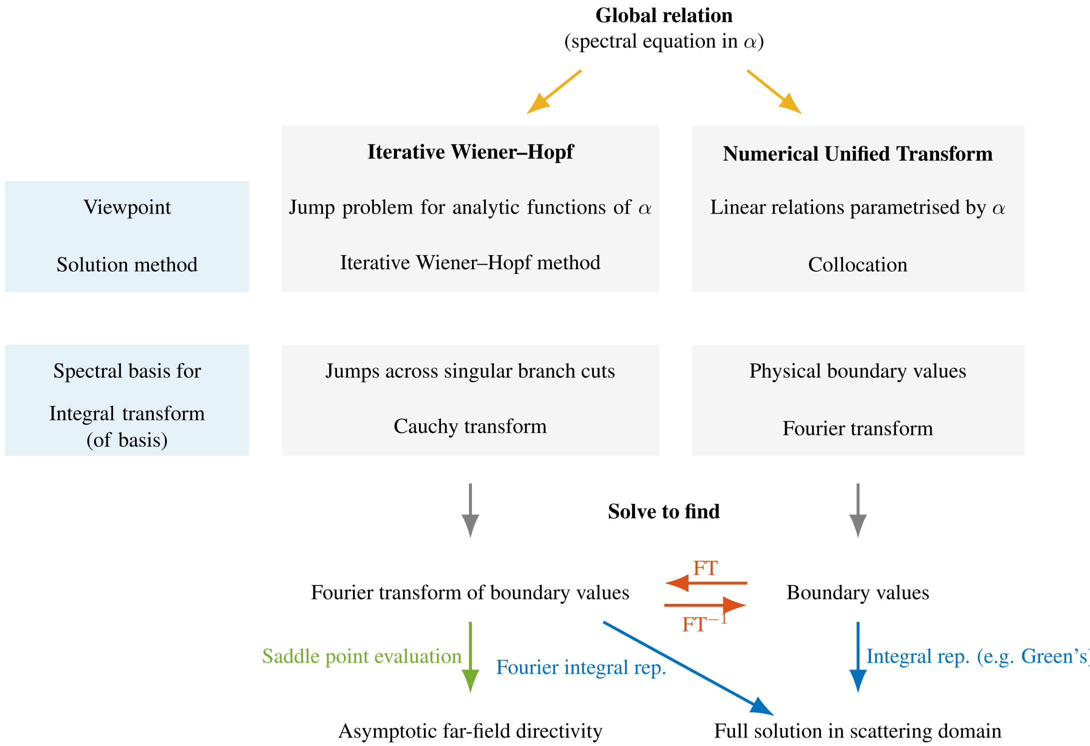

FIG. 3. Illustration of the two numerical methods considered.

closed form expressions for their Cauchy transforms. Whereas the unified transform recovers an expression for the physical boundary values and their Fourier transform, the iterative Wiener–Hopf approach only solves directly for their Fourier transform, and the physical boundary values must be recovered by numerically inverting a Fourier transform. However, the iterative Wiener–Hopf approach is suitable for recovering the far-field directivity using a saddle-point approximation. The entire solution may be recovered using integral representations of the boundary values or their Fourier transform.

The key differences to note are as follows:

- Nature of the functions to be approximated: oscillatory boundary values versus Fourier transform of boundary values, evaluated on steepest descent contour. For the unified transform, the boundary values along each segment of the domain must be represented accurately, typically requiring more degrees of freedom for large wavenumbers. In the iterative Wiener–Hopf method, the Fourier transforms of the boundary values are represented in terms of Cauchy transforms of smooth non-oscillating functions.
- Solution method: collocation of discretized global relation versus iteration of scalar Wiener–Hopf problems associated with scattering events. This means the iterative method is more naturally suited to problems involving large wavenumbers.
- Solution quantity most easily recovered: boundary values (jump over the plates) versus Fourier transform of boundary values (and so far-field directivity) in the iterative Wiener–Hopf method.

We now outline each method and its implementation in more detail, before comparing the performance of each method for multiple plates in § 5.

3. Unified transform

In this section, we briefly discuss the unified transform and how it can be used as a numerical method for scattering problems (Ayton *et al.*, 2019; Colbrook *et al.*, 2019a). For a full discussion of the method applied to elastic plate geometries, we refer the reader to Colbrook & Ayton (2019). The first step is to obtain the so-called 'global relation'. Once the global relation is obtained, we can expand all unknown boundary data in terms of carefully selected basis functions to obtain a linear system for the expansion coefficients. Finally, the linear system can be evaluated at collocation points to solve for the unknown expansion coefficients.

3.1 *The global relation for collinear plates*

The unified transform can be applied to arbitrary elliptic PDEs with constant coefficients (Colbrook *et al.*, 2019a, 2018) and more general separable PDEs (Colbrook, 2020). However, in this paper, we are solely concerned with the Helmholtz scattering problem for the geometry outlined in § 2. We define $\Lambda = (-1,0) \cup (1,\infty) \cup \{e^{i\theta} : \pi < \theta < 2\pi\}$ and let $\beta = k_0/2$. The global relation for our problem (see Colbrook & Ayton, 2019, for a simple derivation using Green's theorem) is

$$\int_{\mathbb{R}\backslash\gamma} e^{-i\beta x(\lambda+\frac{1}{\lambda})} q_y(x,0)\mathrm{d}x + \int_{\gamma} e^{-i\beta x(\lambda+\frac{1}{\lambda})} \left[q_y(x,0) + \frac{\beta}{2}\left(\lambda - \frac{1}{\lambda}\right)[q](x,0)\right]\mathrm{d}x = 0, \qquad \lambda \in \Lambda. \tag{3.1}$$

The idea is to expand the unknowns in this relation in suitable basis functions and evaluate at enough collocations points λ to set up a well-conditioned linear system for the unknown coefficients. In the special case of this collinear geometry, there is another interpretation of the global relation that we wish to highlight. Using the fact that the scattered field is anti-symmetric in the y-direction yields the boundary integral equation

$$\frac{1}{4}[q](x,0) + \int_{\mathbb{R}} G(x-x')q_y(x',0)\mathrm{d}x' = 0, \tag{3.2}$$

where G is the Green's function

$$G(x) = \frac{i}{4}H_0^{(1)}(k_0|x|)$$

and where $H_\alpha^{(1)}(\cdot)$ denotes the Hankel function of the first kind of order α. Taking the Fourier transform of (3.2) with frequency parameter $w = \beta(\lambda + 1/\lambda)$ and using the convolution theorem yields

$$\int_\gamma e^{-i\beta x(\lambda+\frac{1}{\lambda})}[q](x,0)\mathrm{d}x + i\int_{\mathbb{R}} e^{-i\beta x(\lambda+\frac{1}{\lambda})}q_y(x,0)\mathrm{d}x \int_{\mathbb{R}} e^{-i\beta x(\lambda+\frac{1}{\lambda})}H_0^{(1)}(k_0|x|)\mathrm{d}x = 0.$$

Note that the allowed λ values correspond exactly to real w. The Fourier transform of the Hankel function is known (Olver *et al.*, 2010) and yields

$$\mathrm{i}\int_{\mathbb{R}} \mathrm{e}^{-\mathrm{i}\beta x(\lambda+\frac{1}{\lambda})} H_0^{(1)}(k_0\,|x|)\mathrm{d}x = \frac{2}{\beta(\lambda - 1/\lambda)}.$$

It follows that the global relation (3.1) in this case is exactly the Fourier transform of the boundary integral equation (3.2). The convolution with the singular integral is transformed into a multiplication in Fourier space and hence the unified transform avoids the need for difficult quadratures. We should stress that this interpretation as collocating the Fourier transform of boundary integral equations does not hold in generality. However, it does serve as an intuition behind the method for more complicated geometries. Note also that we obtain the same equation when using the Wiener–Hopf method in (4.3) through the formal substitution $\beta(\lambda + \frac{1}{\lambda}) = -\alpha$ and

$$K(\alpha) = \sqrt{\alpha^2 - k_0^2} = \beta\left(\lambda - \frac{1}{\lambda}\right).$$

In other words, we can view the unified transform, in particular the global relation (3.1), as a natural generalization (when considering more complex domains) of Fourier transforms of the boundary integral equations. The method itself can be viewed as a numerical method for solving Wiener–Hopf type problems for arbitrary domains.

3.2 *Basis functions and the approximate global relation*

We split $\mathbb{R}\backslash\gamma$ into the following intervals. Let $\mathcal{I}_1 = (-\infty, x_{1,0})$ and $\mathcal{I}_2 = (x_{M,1}, \infty)$. Then $[x_{1,0}, x_{M,1}]\backslash\gamma$ can be split into disjoint open intervals $\mathcal{J}_i$ for $i = 1, ..., M-1$. For notational convenience, we introduce $L_i = |\gamma_i| = x_{i,1} - x_{i,0}$ and $m_i = (x_{i,1} + x_{i,0})/2$ for $i = 1, ..., M$ as well as $L_i' = |\mathcal{J}_i|$ and m_i' equal to the midpoint of $\mathcal{J}_i$ for $i = 1, ..., M-1$. We suppose that along each plate γ_i we are given a relation of the form

$$q_y(x,0) - \mu_i[q](x,0) = f_i(x),$$

for known functions f_i and parameters μ_i (which when considering the unified transform, we assume to be constant along each plate). The unknowns in the global relation (3.1) are $[q]$ on each interval γ_i and q_y on $\mathcal{I}_1, \mathcal{I}_2$ and on each $\mathcal{J}_i$. For the finite intervals γ_i, in order to capture the square-root type singularities of q near the edge tips we define

$$C_m(t) = \sqrt{1-t^2}\cdot U_m(t), \tag{3.3}$$

where $U_m(\cdot)$ denote Chebyshev polynomials of the second kind. These have the following Fourier transform Olver *et al.* (2010):

$$\int_{-1}^{1} \mathrm{e}^{\mathrm{i}\lambda t}\sqrt{1-t^2}\cdot U_m(t)dt = \frac{(m+1)\mathrm{i}^m\pi}{\lambda} J_{m+1}(\lambda), \tag{3.4}$$

where $J_\alpha(\cdot)$ denotes the Bessel function of the first kind of order α. We expand $[q_i] = [q]$ on γ_i as

$$[q_i](x) \approx \sum_{n=1}^{N_i} a_{i,n} C_{n-1}\left(\frac{2x - 2m_i}{L_i}\right).$$

Similarly, for the $M-1$ intervals $\mathcal{J}_i$ we expand $q_{y,i} = q_y$ as

$$q_{y,i}(x) \approx \sum_{n=1}^{N_i'} b_{i,n} S_{n-1}\left(\frac{2x - 2m_i'}{L_i'}\right),$$

where $S_m(t) = T_m(t)(\sqrt{1-t^2})^{-1}$ and $T_m(\cdot)$ denote Chebyshev polynomials of the first kind. These are chosen to capture the derivatives of the relevant square root type singularity and have

$$\int_{-1}^{1} \mathrm{e}^{\mathrm{i}\lambda t} \frac{T_m(t)}{\sqrt{1-t^2}} \mathrm{d}t = \mathrm{i}^m \pi J_m(\lambda). \tag{3.5}$$

For the semi-infinite intervals $\mathcal{I}_1$ and $\mathcal{I}_2$ we expand (after a relevant affine change of variables) in terms of the Bessel functions $\{J_{\frac{n+1}{2}}(k_0 x)/x\}_{n\geq 0}$. These functions have the advantage of capturing the correct singular behaviour near the plate edges when n is even. They also decay with the correct algebraic rate at infinity and have easy to compute Fourier transforms (Olver *et al.*, 2010):

$$\int_0^\infty \mathrm{e}^{\mathrm{i}\lambda t} \frac{J_\alpha(bt)}{t} \mathrm{d}t = \begin{cases} \frac{\exp(\mathrm{i}\alpha \arcsin(\lambda/b))}{\alpha}, & \text{for } 0 \leq \lambda \leq b \\ \frac{b^\alpha \exp(\alpha\pi \mathrm{i}/2)}{\alpha\left(\lambda + \sqrt{\lambda^2 - b^2}\right)^\alpha}, & \text{for } 0 < b \leq \lambda \end{cases}. \tag{3.6}$$

Explicitly, we approximate $q_{y,0} = q_y$ on $\mathcal{I}_1$ via

$$q_{y,0} \approx \sum_{n=1}^{N_0'} b_{0,n} \frac{J_{\frac{n}{2}}(k_0(x_{1,0} - x))}{x_{1,0} - x}$$

and $q_{y,M} = q_y$ on $\mathcal{I}_2$ via

$$q_{y,0} \approx \sum_{n=1}^{N_M'} b_{M,n} \frac{J_{\frac{n}{2}}(k_0(x - x_{M,1}))}{x - x_{M,1}}.$$

Using the formulae for the relevant Fourier transforms, we thus form an approximate global relation

$$\sum_{i=1}^{M} \sum_{n=1}^{N_i} A_{i,n}(\lambda) a_{i,n} + \sum_{i=0}^{M} \sum_{n=1}^{N_i'} B_{i,n}(\lambda) b_{i,n} \approx -\sum_{i=1}^{M} \int_{\gamma_i} \mathrm{e}^{-\mathrm{i}\beta x(\lambda + \frac{1}{\lambda})} f_i(x) \mathrm{d}x. \tag{3.7}$$

The coefficients $A_{i,n}$ are given by

$$A_{i,n}(\lambda) = \left(\frac{1}{\lambda} - \lambda - \frac{2\mu_i}{\beta}\right) e^{-i\beta m_i(\lambda+1/\lambda)} \frac{n i^{n-1}\pi}{2\left(\lambda+\frac{1}{\lambda}\right)} J_n\left(-\frac{\beta L_i}{2}\left(\lambda+\frac{1}{\lambda}\right)\right).$$

We also have

$$B_{0,n}(\lambda) = e^{-i\beta x_{1,0}(\lambda+1/\lambda)} \int_0^\infty e^{i\beta t(\lambda+1/\lambda)} \frac{J_{\frac{n}{2}}(k_0 t)}{t} dt,$$

$$B_{M,n}(\lambda) = e^{-i\beta x_{M,1}(\lambda+1/\lambda)} \int_0^\infty e^{-i\beta t(\lambda+1/\lambda)} \frac{J_{\frac{n}{2}}(k_0 t)}{t} dt.$$

Finally, for $0 < i < M$, we have

$$B_{i,n} = \frac{L_i' i^{n-1}\pi}{2} e^{-i\beta m_i'(\lambda+1/\lambda)} J_{n-1}\left(-\frac{\beta L_i'}{2}\left(\lambda+\frac{1}{\lambda}\right)\right).$$

We evaluate (3.7) at $C \geq \sum N_i + \sum N_i'$ collocation points $\lambda \in \Lambda$ to set up a linear system for the unknown coefficients (typically with $|C| \sim \sum N_i + \sum N_i'$). This is then inverted in the least-squares sense. Once the coefficients are computed, we can reconstruct approximations of the unknown functions.

As we will see later, when $\mu_i = 0$, the unified transform with the above basis choices converges at least exponentially. However, the introduction of Robin boundary conditions induces (poly-)logarithmic type singularities due to resonance phenomena in the poles of the Mellin symbol. This is a well-studied phenomenon in the PDE literature (Martin & Monique, 1996; Mghazli, 1992). The dominant singularities are still square-root, and hence, the unified transform will converge in this case algebraically with a large order of convergence. See § 6.3 for this effect and another interpretation of the above choice of basis functions in elliptic coordinates as a sine series.

3.3 *Collocation points and obtaining the scattered field*

Unfortunately, in contrast to standard spectral methods (Boyd, 2001), there is no current theory describing the best choices for collocation points.[3] For collocation points $\lambda \in \Lambda$, we chose Halton nodes (scattered points with a lack of regularity used in quasi-Monte Carlo integration) in the interval $(-1, 0)$, minus their reciprocal values in $(1, \infty)$, and points in $\{e^{-i\theta} : 0 < \theta < \pi\}$ with θ corresponding to Halton nodes in $(0, \pi)$. This choice corresponds to sampling frequencies along the entire real line of the Fourier transforms of the relevant functions. The complex collocation points along the unit circle are allowed precisely because the solution satisfies the Sommerfeld radiation condition so that the contribution of Green's identity along the relevant semi-circular arc vanishes in the infinite radius limit (see Spence, 2011). To obtain accurate numerical solutions, we needed to sample these points, and hence, we considered the full complex solution. This sampling corresponds to implementing the boundary conditions that make the boundary value problem well posed.

[3] See Colbrook *et al.* (2019b) for a good choice for bounded convex polygons given as rays in the complex plane, which we cannot adopt here due to the restrictions on the values of λ.

In all of the examples encountered in this paper, the scattered field is an odd function in the y variable. Hence, by considering the reflected Green's function

$$G_R(x,y,x',y') = \frac{1}{4\mathrm{i}}\left(H_0^{(1)}\left(k_0\sqrt{(x-x')^2+(y-y')^2}\right) - H_0^{(1)}\left(k_0\sqrt{(x-x')^2+(y+y')^2}\right)\right),$$

and its normal derivative, we can write

$$q(x,y) = \frac{\mathrm{i}k_0 y}{4}\int_\gamma \frac{H_1^{(1)}(k_0\sqrt{(x-x')^2+y^2})}{\sqrt{(x-x')^2+y^2}}[q](x',0)\mathrm{d}x. \tag{3.8}$$

For points off the union of plates γ, (3.8) can be evaluated rapidly using standard Gaussian quadrature. Near the plates (where the integrand becomes singular) we can use first-order approximations from the computed q and its normal derivative along the plates (Colbrook *et al.*, 2019b). We can also evaluate the far field using steepest descent.

4. An iterative Wiener–Hopf method

In this section, we discuss an alternative approach to scattering problems using an iterative Wiener–Hopf formulation. The method we use was introduced in Kisil & Ayton (2018) and implemented for a set of M collinear finite plates in Priddin *et al.* (2020). A matrix Wiener–Hopf problem is formulated, viewed as a set of coupled scalar problems and then solved by fixed-point iteration. We briefly discuss the key steps and refer the reader to Priddin *et al.* (2020) for details.

4.1 *Matrix Wiener–Hopf equation for collinear plates*

The fundamental equation to be solved is analogous to the global relation (3.1). However, this is typically derived in the context of Wiener–Hopf problems by exploiting the y-anti-symmetry of the scattered field q and Fourier transforming the boundary value problem in the x variable using the convention

$$Q(\alpha,y) = \int_{-\infty}^{\infty} q(x,y)\mathrm{e}^{\mathrm{i}\alpha x}\,\mathrm{d}x. \tag{4.1}$$

The x-Fourier transform $Q(\alpha,y)$ of the general solution $q(x,y)$ satisfying the governing Helmholtz equation and decaying as $|y|\to\infty$ may then be represented as

$$Q(\alpha,y) = \mathrm{sgn}(y)A(\alpha)\mathrm{e}^{-K(\alpha)|y|} \tag{4.2}$$

where $K(\alpha) = \sqrt{\alpha^2-k_0^2}$. Here the branch cuts are taken to be the rays $\{\alpha = \pm k_0 \pm \mathrm{i}s : 0 < s < \infty\}$ parallel to the imaginary axis. For $y=0$ this provides the relationship $Q' + KQ = 0$, where $\frac{\partial Q}{\partial y} \equiv Q'$, and so

$$\int_{\mathbb{R}\setminus\gamma} \mathrm{e}^{\mathrm{i}\alpha x} q_y(x,0)\mathrm{d}x + \int_\gamma \mathrm{e}^{\mathrm{i}\alpha x}\left[q_y(x,0) + K(\alpha)q(x,0)\right]\mathrm{d}x = 0, \tag{4.3}$$

which may be recovered from (3.1) using the substitution $\beta(\lambda + \frac{1}{\lambda}) = -\alpha$ and using the fact that q is an odd function in the y variable (as noted in Colbrook *et al.*, 2019a). We now restrict attention to $y = 0+$. The normal derivative of the scattered field q on each plate is prescribed by the incident field q_I, say

$$Q'_{\gamma_m} = F_{\gamma_m} \qquad\qquad 1 \le m \le M \tag{4.4}$$

where F_γ denotes the Fourier transform of a function f along the contour γ. We rewrite equation (4.3) as

$$\sum_{m=1}^{M} \left(KQ_{\gamma_m} + F_{\gamma_m} \right) + Q'_{\mathcal{I}_1} + Q'_{\mathcal{I}_2} + \sum_{m=1}^{M-1} Q'_{\mathcal{J}_m} = 0. \tag{4.5}$$

This is the fundamental equation to be solved that relates Fourier transforms of unknown boundary values. In order to apply the iterative Wiener–Hopf technique we must identify the analyticity and growth at infinity of each term in the upper and lower half planes, annotating those analytic in the upper half plane by $+$ and the lower half plane by $-$. Further, to be consistent with the original paper describing this method, we shall relabel the end points of the plates as $x_1, x_2, ..., x_{2M}$, i.e. $x_{i,0} \to x_{2i-1}$ and $x_{i,1} \to x_{2i}$ for $i = 1, ..., M$. We first denote the unknown functions by

$$V_1 = Q'_{\mathcal{I}_1}, \quad V_{2m+1} = Q'_{\mathcal{J}_m} \text{ for } m = 1, ..., M-1, \quad V_{2M+1} = Q'_{\mathcal{I}_2}, \quad V_{2m} = Q_{\gamma_m} \text{ for } m = 1, ..., M \tag{4.6}$$

and then to ensure $+$ and $-$ functions do not grow exponentially in their half-plane of analyticity we define the shifted functions

$$\Psi_-^{(m)} = \mathrm{e}^{-\mathrm{i}\alpha x_m} V_m \tag{4.7a}$$

$$\Psi_+^{(m)} = \mathrm{e}^{-\mathrm{i}\alpha x_m} V_{m+1} \tag{4.7b}$$

for $1 \le m \le 2M$, each $\Psi_-^{(m)}$ now having algebraic behaviour in the lower half plane, and $\Psi_+^{(m)}$ in the upper half plane. We may now find an $2M \times 2M$ matrix Wiener–Hopf system suitable for the iterative scheme as follows. The m^{th} row may be obtained from equation (4.5) by rescaling by $\mathrm{e}^{-\mathrm{i}\alpha x_m}$ and recasting in terms of $\Psi_\pm$. We find

$$H\Psi_- + G\Psi_+ = F \tag{4.8}$$

where H and G are triangular matrices with entries given by

$$H_{lm} = \begin{cases} 0 & l < m \\ E^{(l,m)} & m \text{ odd and } l \ge m \\ E^{(l,m)}K(\alpha) & m \text{ even and } l \ge m \end{cases}, \quad G_{lm} = \begin{cases} 0 & l > m \\ E^{(l,m)}K(\alpha) & m \text{ odd and } l \le m \\ E^{(l,m)} & m \text{ even and } l \le m \end{cases} \tag{4.9}$$

where $E^{(l,m)} \equiv \mathrm{e}^{\mathrm{i}(x_m - x_l)\alpha}$. The forcing term F is given by

$$F^{(m)} = -\mathrm{e}^{-\mathrm{i}\alpha x_m} \sum_{l=1}^{M} F_{\gamma_l}. \tag{4.10}$$

This formulates a matrix Wiener–Hopf equation where a partial matrix factorization has been achieved to ensure all terms involving unknown functions are analytic with algebraic behaviour at infinity in the upper or lower half planes.

4.2 *Solution by iteration*

We now look to solve equation (4.8) by constructing a fixed-point iteration scheme. The $(2m+1)^{\text{th}}$ row of the matrix equation (4.8) is

$$\begin{aligned}&\sum_{l=1}^{m+1} E^{(2m+1,2l-1)}\Psi_-^{(2l-1)} + \sum_{l=1}^{m} E^{(2m+1,2l)}K\Psi_-^{(2l)}\\ &+\sum_{l=m+2}^{M+1} E^{(2m+1,2l-1)}\Psi_+^{(2l-1)} + \sum_{l=m+1}^{M} E^{(2m+1,2l)}K\Psi_+^{(2l)} = F^{(m)}.\end{aligned} \tag{4.11}$$

We solve at the r^{th} iterative step by considering

$$\begin{aligned}\Psi_-^{(2m+1),r} + K\Psi_+^{(2m+2),r} = &-\sum_{l=1}^{m} E^{(2m+1,2l-1)}\Psi_-^{(2l-1),r-1} - \sum_{l=1}^{m} E^{(2m+1,2l)}K\Psi_-^{(2l),r-1}\\ &-\sum_{l=m+2}^{M+1} E^{(2m+1,2l-1)}\Psi_+^{(2l-1),r-1} - \sum_{l=m+2}^{M} E^{(2m+1,2l)}K\Psi_+^{(2l),r-1} + F^{(m)}\end{aligned} \tag{4.12}$$

where $\Psi_\pm^{(m),r}$ denotes the estimate of $\Psi_\pm^{(m)}$ at the r^{th} solution step, and $\Psi_\pm^{(m),0} = 0$. An analogous equation may be found for even rows. Since the terms on the right-hand side are known, equation (4.12) may be solved by the standard scalar Wiener–Hopf technique. This solution may then be used to update the ‘forcing’ in the remaining rows of the matrix equation. We initialize the scheme by setting unknown terms on the left-hand side to vanish. The iteration sequence may be terminated when an appropriate error threshold between consecutive iterations is reached.

4.3 *Numerical implementation*

The problem has been reduced to solving a sequence of scalar Wiener–Hopf problems of the form

$$K\Psi_+ + \Psi_- = F, \tag{4.13}$$

which are well understood. Using exact scalar multiplicative factorizations of $K = K^+K^-$ and additive Wiener–Hopf factorizations, we may represent the solution in terms of Cauchy transforms along appropriately chosen contours (Noble, 1988). We define the branch cuts of $K(\alpha)$ to be parallel to the imaginary axis in order to be paths of steepest descent of the exponential factors $e^{i\alpha x_m}$. By deforming the Cauchy integration contours onto these branch cuts, we induce square root endpoint singularities at both ends of the branch cut in the integrand. All the Cauchy transforms that must be computed are then of the form

$$\int_0^\infty \frac{f(z)}{z^{1/2}(z-\alpha)}\mathrm{d}z \tag{4.14}$$

where f is a smooth, non-oscillatory function on $(0,\infty)$ decaying as $z\to\infty$. To evaluate such singular integrals numerically, we first relate the Cauchy transform on the half-line to one on the finite interval $(-1,1)$ with similar endpoint and non-oscillatory behaviour using a Möbius map (Trogdon & Olver, 2016). We then employ the spectral approach to Cauchy transforms introduced in Olver (2011) and implemented in the programming language Julia in Slevinsky & Olver (2017), encoding the square root endpoint singularities through the weight $(1-x^2)^{-1/2}$ of 'modified' Chebyshev polynomials $T_n^z(\cdot)$ on $(-1,1)$ introduced in Trogdon & Olver (2016). Specifically, we define $T_n^z(x)$ by

$$T_0^z(x)=1,\quad T_1^z(x)=x,\quad T_n^z(x)=T_n(x)-T_{n-2}(x),\quad n\geq 2 \tag{4.15}$$

where the $T_n(\cdot)$ are Chebyshev polynomials of the first kind. The associated moments of the Cauchy transform on $(-1,1)$ have simple expressions in terms of elementary functions. The application of the iterative scheme may then be cast in terms of fast transforms between function values and coefficients on the branch cuts, and the evaluation of Cauchy transforms by contracting matrices of precomputed Cauchy transform moments with vectors of coefficients. In Llewellyn Smith & Luca (2019), where the Wiener–Hopf problems for scattering by a half-plane is considered numerically, the square root endpoint singularities in the spectral function Q (Φ in Llewellyn Smith & Luca, 2019) on a doubly infinite interval are encoded through the use of rational mappings that have multiple inverses. Since we only consider semi-infinite rays (having deformed a doubly infinite interval onto each side of a semi-infinite branch cut), we avoid this complication.

While a small number of degrees of freedom are typically required to approximate a function with given exponential or algebraic decay by tuning the mapping, for ease of implementation, we consider a single mapping for all cases. Therefore the present implementation requires more degrees of freedom for problems involving high and low wavenumbers, and those involving larger numbers of plates; this is associated with approximating a range of different exponential decay rates.

To recover the spatial field $q(x,y)$ we must invert the x-Fourier transform (4.1):

$$q(x,y)=\frac{\mathrm{sgn}(y)}{2\pi}\int_{-\infty}^{\infty} Q(\alpha,0+)\mathrm{e}^{-\mathrm{i}\alpha x-K(\alpha)|y|}\,\mathrm{d}\alpha \tag{4.16}$$

Again, the asymptotic far field may be readily recovered by the method of steepest descent. For evaluation of the far field in or near the direction of the reflected wave, one must take care of the removable singularity in the spectral forcing term F. One approach is to compute Q using the Cauchy integral formula.

5. Analysis of methods for multiple plates

We now compare the two spectral methods for scattering by a set of collinear finite sound-hard plates. All experiments in this section were performed with an incident field given by (2.3) with $\theta=\pi/4$. It is of primary interest to quantify performance at different wavenumbers and plate numbers in order to identify which method should be preferred. It is also pertinent to highlight a number of qualitative points

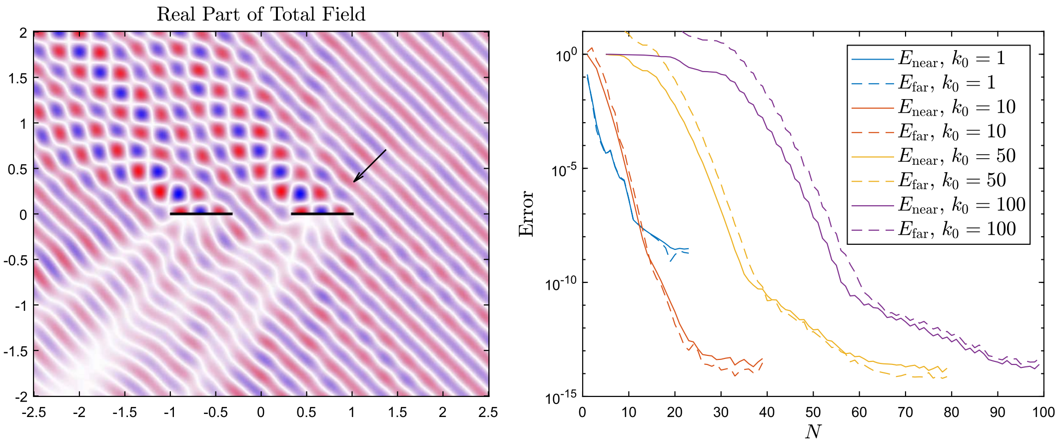

FIG. 4. Left: Example computed total field for $k_0 = 50$. Right: Exponential convergence of the unified transform (near field and far field) for different k_0.

regarding performance differences for obtaining different aspects of the solution, ease of implementation and adaptability.

We start with the case of two equally spaced plates with $d = 2a = 2/3$ in the interval $[-1, 1]$. Figure 4 (left) shows the total computed field for $k_0 = 50$. To measure error, we will consider both the near field and the far field. For the near field, we compute an approximation $[\tilde{q}]$ to $[q]$, the jump in q across the plates, at equally spaced points $\{x_j\} \subset \gamma$ and define

$$E_{\rm near} = \frac{\sum_j \left|[\tilde{q}](x_j, 0) - [q](x_j, 0)\right|}{\sum_j \left|[q](x_j, 0)\right|}. \tag{5.1}$$

The unified transform computes $[\tilde{q}]$ via a series expansion, whereas the iterative Wiener–Hopf method obtains $[\tilde{q}]$ from the inverse Fourier transform of $\tilde{Q}$ (an approximation of Q), which we compute using Gaussian quadrature. For the far field, the asymptotic form of the solution can be computed via steepest descent applied to the Fourier inversion integral to obtain

$$q(r, \theta) \sim \mathrm{e}^{ik_0 r} \sin\theta \sqrt{\frac{k_0}{2\pi r}} \int_\gamma \mathrm{e}^{-ik_0 x \cos\theta} q(x, 0+)\mathrm{d}x, \quad \text{as} \quad r \to \infty, \tag{5.2}$$

where (r, θ) are the usual polar coordinates. The quantity $D(\theta)$ is defined by

$$D(\theta) = \sin\theta \int_\gamma \mathrm{e}^{-ik_0 x \cos\theta} q(x, 0+)\mathrm{d}x$$

so that (5.2) becomes

$$q(r,\theta) \sim \mathrm{e}^{ik_0 r}\sqrt{\frac{k_0}{2\pi r}}D(\theta), \quad \text{as} \quad r \to \infty.$$

Note that the finite extent of the plates means that the Fourier transform of q is pole free; poles would give rise to Fresnel regions and require special treatment to achieve a uniformly valid expression (in our case the far field is beyond the Rayleigh distance). We compute an approximation $\tilde{D}$ to D at equally spaced angles $\{\theta_j\} \subset (0,\pi)$ and define

$$E_{\mathrm{far}} = \frac{\sum_j \left|\tilde{D}(\theta_j) - D(\theta_j)\right|}{\sum_j \left|D(\theta_j)\right|}.$$

Note that $\tilde{D}$ can be computed using the unified transform and the relevant Fourier transforms (see (3.4)) of the functions $\{C_m\}$ (defined in (3.3)), whereas the iterative Wiener–Hopf method directly computes these Fourier transforms at points of interest. In reality, we do not have access to the true scattered field q to compute the above errors. Hence we will use a 'converged' solution (computed using a larger number of degrees of freedom). In what follows, E_{near} was computed using 201 evenly spaced points on each plate and E_{far} was computed using 99 evenly-spaced angles.

Figure 4 (right) shows the exponential convergence of the unified transform for different wavenumbers k_0 and $N_i = N_i' = N$. As discussed in Colbrook & Ayton (2019), we found that for larger k_0, larger N is needed before we see exponential convergence. This is due to the more oscillatory solution and typically the N needed to gain a given accuracy scales linearly with k_0. However, we also see another effect. For small $k_0 = 1$, the convergence is slower, plateauing at a larger relative error $\approx 10^{-9}$. This can be overcome by increasing the number of collocation points and, for the examples in this paper, was not an issue in practice. There does seem to be an inherent ill-conditioning of (3.1) and equivalently (4.3) for smaller k_0, which can be understood as a consequence of the branch points of $K(\alpha)$ coalescing. Another interpretation is the slower decay properties of the solution at infinity—the unified transform expands the y-derivative of the scattered field along the infinite portions of $\mathbb{R}\backslash\gamma$, whereas the iterative Wiener–Hopf method involves integrands that decay at a slower rate for smaller k_0. Also, in the case of small k_0, it is well known that the large incompressible region around a screen causes numerical difficulties. There is a large amount of energy in this region compared to the scattered field, and hence standard numerical methods must resolve both regimes. This difficulty highlights the importance of boundary approaches such as the ones we present, which can capture such behaviour.

Figure 5 shows the exponential convergence of the iterative Wiener–Hopf method. There are two key parameters in the numerical implementation of the iterative stage of the method: the number of degrees of freedom used to compute the Cauchy transforms using the spectral approach described in § 4.3, and the number of iterations undertaken before the solution is extracted. The left-hand panel of Fig. 5 demonstrates that the method converges exponentially in the number of degrees of freedom, and the right-hand panel that the method converges exponentially in the number of iterations. For the present implementation, the number of degrees of freedom required to obtain a given accuracy increases outside an optimal regime centred near and around $k_0 = 10$. This is associated with the need to approximate smooth functions with a range of decay rates; for ease of implementation, we consider a single quadrature scheme that can still provide a high degree of accuracy for a range of wavenumbers with around 100 degrees of freedom. Convergence with iteration is fastest for high wavenumbers.

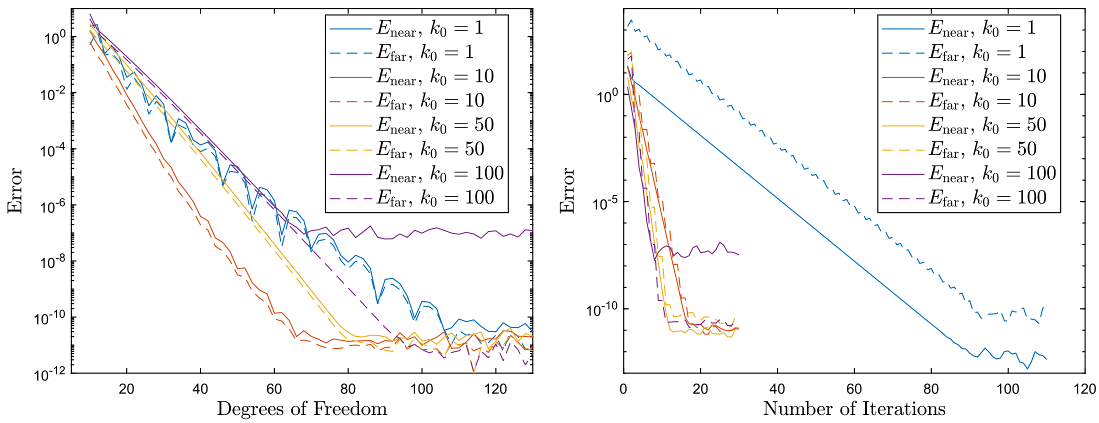

FIG. 5. Left: Exponential convergence in degrees of freedom used for computing factorizations using Cauchy transforms of the iterative Wiener–Hopf method (near field and far field) for different k_0. Right: Exponential convergence in iteration of the iterative Wiener–Hopf method (near field and far field) for different k_0.

As mentioned previously, obtaining the near field requires more care for large wavenumbers using the iterative approach due to issues around inverting the x-Fourier transform of functions with strong exponential behaviour, while also choosing a contour to avoid the branch points at $\pm k_0$. This difficulty is evidenced for the case of $k_0 = 100$ in each panel where the method struggles to achieve more than seven digits of accuracy (compared to about 14 digits obtained with the unified transform). Should particular applications require higher accuracy, specialization might mitigate these issues. The inversion method employed uses a single contour for each spatial location, which means errors are largest at angles $\pm\pi/2$ and $0, \pi$ from each plate edge.

Though each method converges exponentially, we found that when computing the far field, the iterative Wiener–Hopf method scales better for large frequencies. On the other hand, both methods perform similarly for smaller k_0. This is shown in Fig. 6 (left) where we have shown the time taken[4] by each method to reach $E_{far} < 10^{-4}$ for a single plate between $[-1, 1]$. The unified transform is more appropriate for computing the near field (as shown in Fig. 5), and so we have measured the error via E_{far}. We have also compared the time taken to reach $E_{far} < 10^{-4}$ for different values of M (number of plates) with $d = 2a$ in Fig. 6 (right) for $k_0 = 2$. In this case, we see that the unified transform is slightly faster, though both methods seem to scale with the same algebraic rate (roughly cubically). Finally, we compare the computation time to gain $E_{far} \leq 10^{-2}$ for 20 plates with $k_0 = 2$ and different open fractions $2a/d$ in Fig. 7. The unified transform fares much better than the iterative Wiener–Hopf method when $2a/d$ is small, with a much slower increase in computation time as $2a/d$ decreases (the step shape for the unified transform is due to the increasing number of basis functions needed). This agrees with Priddin *et al.* (2020) where it was noted that the number of iterations required to achieve a given degree of accuracy is strongly correlated with the smallest Helmholtz number (wavenumber $\times$ lengthscale) present in the problem.

[4] All timings were performed using the BenchmarkTools.jl package on a 2018 MacBook Pro, a 2.3Ghz processor and 8GB memory, with the figures quoting the mean time from each trial.

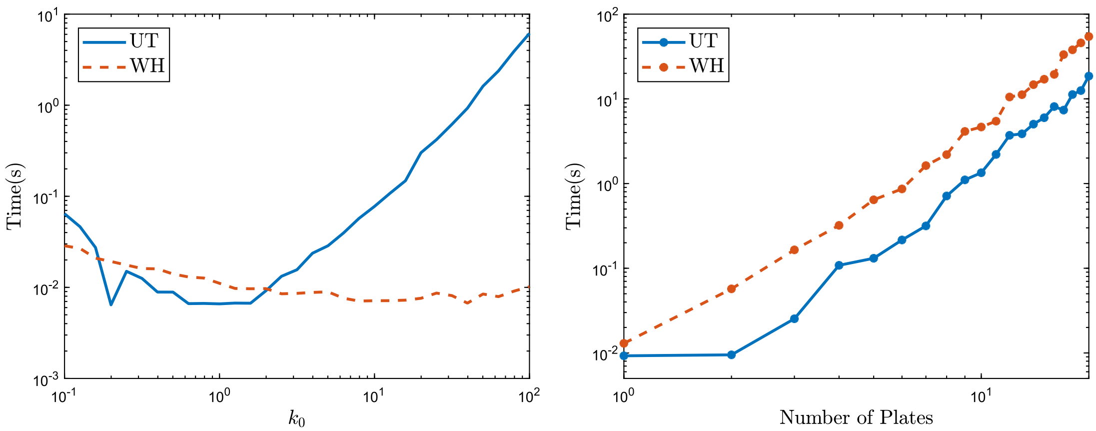

FIG. 6. Average time taken to achieve four digits of accuracy in the far-field directivity $\tilde{D}$ using unified transform (solid blue) and iterative Wiener–Hopf method (dashed red). Left: Single plate with endpoints at $[-1, 1]$ for different wavenumbers k_0. Right: M plates with plate length and spacing all equal, with extreme endpoints at $\{-1, 1\}$ for wavenumber $k_0 = 2$.

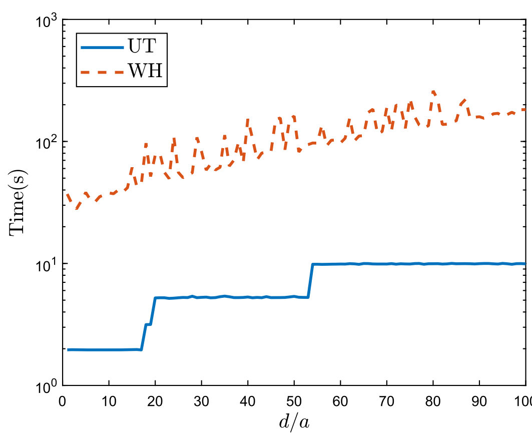

FIG. 7. Average time taken to achieve two digits of accuracy in the far-field directivity $\tilde{D}$ using unified transform (solid blue) and iterative Wiener–Hopf method (dashed red) for twenty plates ($M = 20$) and $k_0 = 2$. We have plotted against d/a as opposed to the open fractions $2a/d$ since this best shows the growth in time taken.

In summary:

- Both methods converge exponentially in the number of degrees of freedom used.
- Both methods offer similar scaling (computation time) as the number of plates is increased.
- The unified transform is better suited for computing the spatial field, especially on or near the domain boundary, since the solution is represented in physical space.
- The iterative Wiener–Hopf method is better suited to large wavenumbers and generally appears to be less sensitive to changes in the wavenumber.

- The time taken for the iterative Wiener–Hopf method depends strongly on the smallest Helmholtz number (and so lengthscale) present and the method is therefore much slower than the unified transform when the open fraction $2a/d$ is small.
- The unified transform requires care in choosing the basis functions for the unknowns (in our case the functions in (3.3) to capture endpoint singularities) and also the collocation points.
- The iterative Wiener–Hopf method requires care in order to cope with singular features, such as singularities of the solution (captured by the orthogonal weights of the Chebyshev polynomials), evaluation near removable singularities and conducting effective spatial inversion. There is also a need to balance the number of iterations with the degrees of freedom. For the problems considered, 400 degrees of freedom are typically sufficient, and we iterate until a prescribed relative error between iterates is reached.

Finally, in general, the unified transform is more versatile and able to cope with more complicated geometries. We will use the unified transform to compute the near field in § 7.1 and both methods for the far field (in order to verify computations) in § 7.2.

6. A collocation method for a single compliant plate

In this section, we discuss the numerical solution of the scattering by a *single* plate $x \in [-1, 1]$ with Robin boundary conditions. Our solution will be obtained via a mixture of separation of variables and collocation. The geometry of a single plate can be transformed into a separable PDE on a rectangular domain. Essentially, a flat plate can be considered as a degenerate ellipse of zero thickness (Morse & Rubenstein, 1938). The solution can be written down as an infinite series of Mathieu functions, the appropriate eigenfunctions, the theory of which can be found in McLachlan (1951). Separation of variables yields the solution everywhere in the domain and not just the unknown boundary values, bypassing the need for Green's representation theorem or steepest descent to evaluate the solution in the exterior domain. Of course, we must still numerically sum a series of special functions, which can be represented efficiently using series representations, as shown below.

6.1 *Separation of variables*

The first few steps, which we recall for the benefit of the reader, are standard for the case of $\mu \equiv 0$ and can be found, e.g. in Colbrook *et al.* (2019a); Nigro (2017). First, we introduce elliptic coordinates via $x = \cosh(\nu)\cos(\eta), y = \sinh(\nu)\sin(\eta)$, where, with an abuse of notation, we write $q(\nu, \eta)$, $\mu(\eta)$ and $f(\eta)$. The appropriate domain then becomes $\nu \geq 0$ and $\eta \in [0, \pi]$ and the PDE, boundary conditions and radiation condition become

$$\begin{cases} \frac{\partial^2 q}{\partial \eta^2} + \frac{\partial^2 q}{\partial \nu^2} + \frac{\cosh(2\nu) - \cos(2\eta)}{2} k_0^2 q = 0, \\ q|_{\eta=0} = q|_{\eta=\pi} = 0, \\ \frac{1}{\sin(\eta)} \frac{\partial q}{\partial \nu}(0, \eta) - 2\mu(\eta) q(0, \eta) = f(\eta), \\ \lim_{\nu \to \infty} \nu^{1/2} \left(\frac{\partial}{\partial \nu} - \mathrm{i}k_0\right) q(\nu, \eta) = 0. \end{cases} \tag{6.1}$$

To simplify the formulae, we let $Q = k_0^2/4$. Separation of variables for solutions of the form $V(\nu)W(\eta)$ leads to the regular Sturm–Liouville eigenvalue problem

$$\begin{cases} W''(\eta) + (\lambda - 2Q\cos(2\eta))\,W(\eta) = 0, \\ W(0) = W(\pi) = 0. \end{cases} \tag{6.2}$$

The solutions of this are sine-elliptic functions, denoted by se_m with eigenvalue λ_m, which we expand as

$$\mathrm{se}_m(\lambda_m, \eta) = \sum_{l=1}^{\infty} B_l^{(m)} \sin(l\eta). \tag{6.3}$$

The eigenfunctions are real and orthogonal, and we choose the normalization

$$\int_0^\pi \mathrm{se}_m(\eta)\mathrm{se}_n(\eta)\mathrm{d}\eta = \frac{\pi}{2}\delta_{mn}. \tag{6.4}$$

We also split the solutions further by symmetry or antisymmetry about $\eta = \pi/2$ and write

$$\mathrm{se}_{2m}(\eta) = \sum_{l=1}^{\infty} B_{2l}^{(2m)} \sin(2l\eta), \tag{6.5}$$

$$\mathrm{se}_{2m+1}(\eta) = \sum_{l=0}^{\infty} B_{2l+1}^{(2m+1)} \sin((2l+1)\eta). \tag{6.6}$$

For the even order solutions, the eigenvalue problem then becomes the tridiagonal system

$$\begin{pmatrix} 2^2 - \lambda_{2m} & Q & & & \\ Q & 4^2 - \lambda_{2m} & Q & & \\ & Q & 6^2 - \lambda_{2m} & Q & \\ & & \ddots & \ddots & \ddots \end{pmatrix} \begin{pmatrix} B_2^{(2m)} \\ B_4^{(2m)} \\ B_6^{(2m)} \\ \vdots \end{pmatrix} = 0. \tag{6.7}$$

A similar system holds for the odd order solutions:

$$\begin{pmatrix} 1^2 - \lambda_{2m+1} - Q & Q & & & \\ Q & 3^2 - \lambda_{2m+1} & Q & & \\ & Q & 5^2 - \lambda_{2m+1} & Q & \\ & & \ddots & \ddots & \ddots \end{pmatrix} \begin{pmatrix} B_1^{(2m+1)} \\ B_3^{(2m+1)} \\ B_5^{(2m+1)} \\ \vdots \end{pmatrix} = 0. \tag{6.8}$$

These eigenvalue problems are solved using square $n \times n$ truncations of the infinite matrix (also known as the finite section method or Galerkin method). Since the spectrum of the associated (self-adjoint) linear operator is discrete, we do not have to worry about issues such as spectral pollution (Colbrook *et al.*, 2019c; Lewin & Séré, 2010).

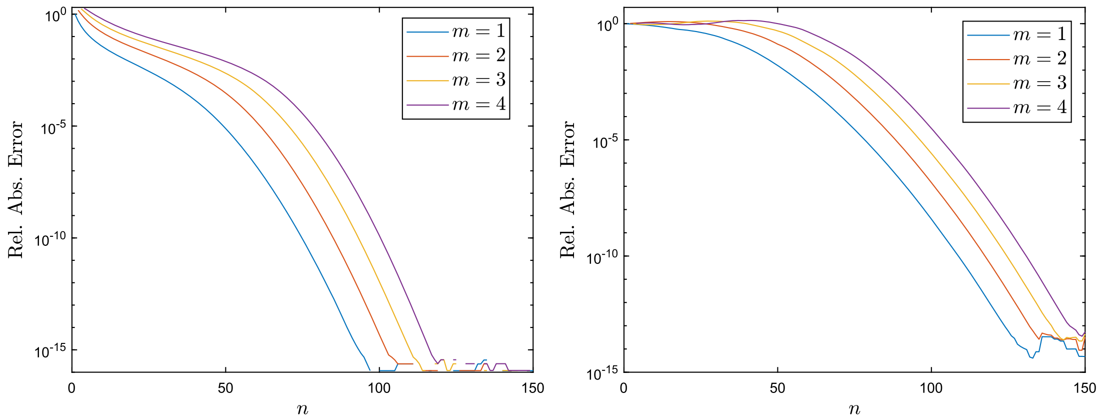

FIG. 8. Convergence results for the finite section method for even order system (6.7) with $k_0 = 1000$. Left: Relative absolute error for first four eigenvalues. Right: Maximum relative absolute error over $\eta \in [0, \pi]$ for first four eigenfunctions.

The convergence to the eigenvalues and eigenfunctions depends on the parameter Q, in general being slower for larger Q. However, the convergence is exponential, yielding machine precision for small truncation parameter n, even for very large Q. Figure 8 shows the convergence for $Q = 250,000$, corresponding to $k_0 = 1000$—at least an order of magnitude larger than those considered in the rest of this paper. Typically for the parameter regimes discussed in this paper, a few dozen sine functions are enough to yield machine precision.

The corresponding $V(\nu)$ with the appropriate radiation condition at infinity are given by the Mathieu–Hankel functions

$$\mathrm{Hse}_m(\nu) = \mathrm{Jse}_m(\nu) + \mathrm{i}\mathrm{Yse}_m(\nu),$$

where Jse_m and Yse_m denote radial Mathieu functions (Olver *et al.*, 2010). These can be expanded in a rapidly convergent series using Bessel functions (see McLachlan, 1951). We choose the normalization $\mathrm{Hse}'_m(0) = 1$ and the full solution can then be written as

$$q(\nu, \eta) = \sum_{m=1}^{\infty} a_m \mathrm{se}_m(\eta)\mathrm{Hse}_m(\nu).$$

In order to determine the coefficients $\{a_m\}$, we need to use the Robin boundary conditions. These boundary conditions yield the relation

$$\sum_{m=1}^{\infty} a_m \mathrm{se}_m(\eta)\left[1 - 2\mu(\eta)\mathrm{Hse}_m(0)\sin(\eta)\right] = \sin(\eta)f(\eta). \tag{6.9}$$

6.2 *Numerical approach*

For non-zero μ, there are at least two natural ways to proceed. We can truncate the relation (6.9) to N terms and collocate at $\eta \in [0, \pi]$. Another option is to multiply by $\mathrm{se}_n(\eta)$ and integrate along the interval $\eta \in [0, \pi]$, using the orthogonality of the sine-elliptic functions. For each $n = 1, ..., N$, this second approach yields the approximate linear relation

$$a_n - \frac{4}{\pi}\sum_{m=1}^{N} a_m \mathrm{Hse}_m(0)\int_0^{\pi} \mu(\eta)\mathrm{se}_m(\eta)\mathrm{se}_n(\eta)\sin(\eta)\mathrm{d}\eta = \frac{2}{\pi}\int_0^{\pi} \sin(\eta)\mathrm{se}_n(\eta)f(\eta)\mathrm{d}\eta. \tag{6.10}$$

Both of these approaches lead to a dense linear system and this is the price we pay for the more complicated boundary conditions (the system becomes diagonal when $\mu = 0$). When μ is constant, we can easily evaluate the relevant integrals in (6.10) to machine precision. For example,

$$\int_0^{\pi} \mathrm{se}_m(\eta)\mathrm{se}_n(\eta)\sin(\eta)d\eta = \sum_{l,k=1}^{\infty} B_l^{(m)}B_k^{(n)}\int_0^{\pi} \sin(l\eta)\sin(k\eta)\sin(\eta)d\eta \tag{6.11}$$

$$= \sum_{l,k=1}^{\infty} B_l^{(m)}B_k^{(n)} \begin{cases} \frac{2kl\left((-1)^{k+l}+1\right)}{4k^2l^2-(k^2+l^2-1)^2}, & \text{if } |k-l| \neq 1 \\ 0, & \text{otherwise} \end{cases}. \tag{6.12}$$

The typical forcing term corresponding to (2.3) can be written in terms of Bessel functions as

$$\frac{2}{\pi}\int_0^{\pi} \sin(\eta)\mathrm{se}_n(\eta)f(\eta)\mathrm{d}\eta = \frac{2}{\pi}\mathrm{i}k_0\sin(\theta)\sum_{l=1}^{\infty} B_l^{(n)}\int_0^{\pi} \sin(\eta)\sin(l\eta)\mathrm{e}^{-\mathrm{i}k_0\cos(\theta)\cos(\eta)}\mathrm{d}\eta \tag{6.13}$$

$$= -2\tan(\theta)\sum_{l=1}^{\infty} \mathrm{i}^{-l} l B_l^{(n)} J_l(k_0\cos(\theta)). \tag{6.14}$$

However, unless μ lends itself to integration against a triple product of highly oscillatory sine functions, the integrals in the left-hand side of (6.10) are very difficult to evaluate numerically for large m, n. One approach is to expand μ in a sine series using the FFT and use formulae for integrating quadruple products of sine functions. Instead, we shall take the simpler approach of truncating (6.9) to N terms and collocating at N equally spaced points in $[0, \pi]$. In physical space, this corresponds to collocation at Chebyshev nodes.

6.3 *Verification of methods*

We now verify that our computational method converges. We will measure the error via the same discrete relative absolute error in (5.1) but now over 199 equally spaced points in the interval $[-1, 1]$. Figure 9 (left) shows the convergence of separation of variables (both collocation and Galerkin matrix), as well as the unified transform for $\theta = \pi/4, k_0 = 10, M = 10$ and $2a/d = 0.2$ with the constant choice (see (2.6))

$$\mu_0 = \frac{\pi}{2d}\left\{\log\left(d/\pi a\right)\right\}^{-1}.$$

We see that all three methods are comparable in terms of convergence with N. As noted earlier at the end of § 3.2, we also see that the convergence is now algebraic owing to the Robin boundary conditions (and induced (poly-)logarithmic singularities). The rate of convergence is large since the dominant singularity of the solutions is square-root at the endpoints, which is still captured by our choice of basis. The

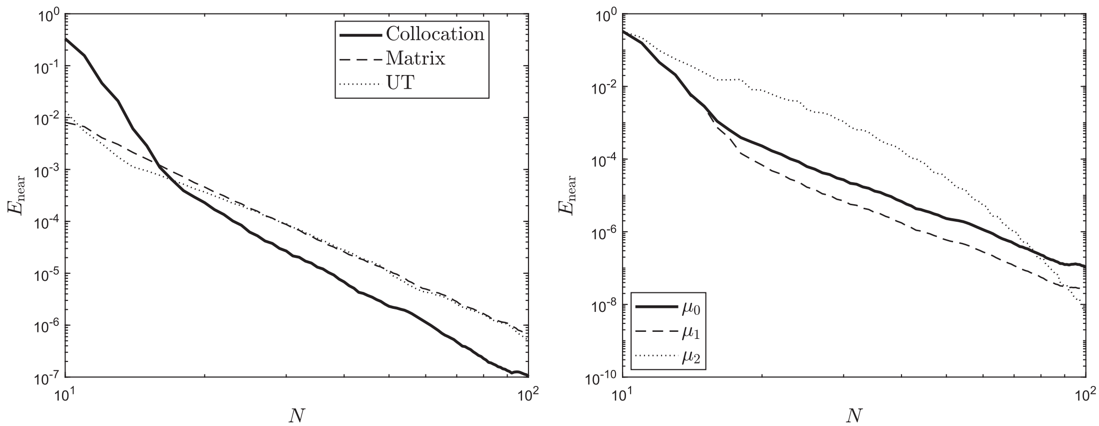

FIG. 9. Left: Convergence of the collocation method, direct matrix method and unified transform for constant μ_0. Right: Convergence of collocation method for μ_0, μ_1 and μ_2.

agreement between the unified transform and separation of variables can be understood in terms of basis functions

$$\sqrt{1-x^2} \cdot U_m(x) = \sin((m+1)\eta).$$

These sine functions also appear in (6.3), however as an infinite expansion. Despite this, we see the same qualitative convergence. Out of all three methods, the collocation approach is the most accurate with very stable convergence rates.

In order to consider the effect of varying the compliance near the extreme endpoints, as speculatively suggested in Leppington (1977), we will also use two ways of tapering μ to 0 at the endpoints, shown in Fig. 10. The first, μ_1, will decay to zero like $1/\log(1/(|x^2-1|))$ at the end points, whereas the second, μ_2, will decay to zero exponentially fast near the endpoints (specifically using a tanh function). For both of these, the envelope of decay was chosen to be of the order d, consistent with the physical picture (we found this to be more accurate than other decay length-scales such as a). Specifically, we take

$$\tilde{\mu}_1^{-1}(x) = \log\left(\frac{d+(x+1)}{a\pi\frac{x+1}{d}}\right) + \log\left(\frac{d+(1-x)}{a\pi\frac{1-x}{d}}\right) - \log\left(\frac{d}{a\pi}\right), \quad \mu_1(x) = \mu_0\frac{\tilde{\mu}_1(x)}{\tilde{\mu}_1(0)}, \tag{6.15}$$

$$\tilde{\mu}_2(x) = \tanh\left(3\frac{(x+1)-d}{d}\right) + \tanh\left(3\frac{(1-x)-d}{d}\right), \quad \mu_2(x) = \mu_0\frac{\tilde{\mu}_2(x)-\tilde{\mu}_2(-1)}{\tilde{\mu}_2(0)-\tilde{\mu}_2(-1)}. \tag{6.16}$$

The functions $\tilde{\mu}_1$ and $\tilde{\mu}_2$ describe the qualitative shape of the compliances. The choice of μ_1 is motivated by the analysis in Lamb (1895) but now has the correct limiting value of $\mu = 0$ at the endpoints.

The convergence of the collocation method, in these cases, is shown in Fig. 9 (right) where we see algebraic convergence for μ_1 but exponential convergence for μ_2 owing to the rapid decay of μ_2 near the endpoints. For our comparison between Robin boundary conditions and the perforated screen, the several digits typically obtained when $N = 100$ are easily sufficient for our purposes. Smaller errors can be obtained for larger N if desired.

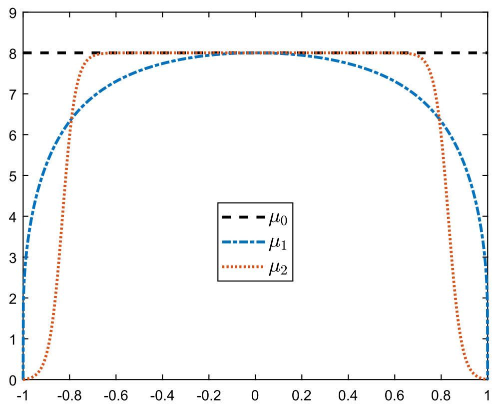

FIG. 10. Examples of μ for ten plates between $[-1, 1]$ with $2a/d = 0.2$.

7. Robin boundary condition versus small rigid plates

Now that we have discussed our numerical methods, and shown them to be effective for the considered problem, we turn to the application that motivated this paper, namely, the investigation of (2.4). We will begin with the near field, where we use the unified transform (which is easier to compute the near field with than the iterative Wiener–Hopf method) and note that we do not expect small errors very near the plate. In fact, we expect large errors near the plates up to distances of approximately $\mathcal{O}(d)$. We then move onto the acoustic far field where we use both the unified transform and the iterative Wiener–Hopf method to verify our numerical computations. However, the computation when $2a/d$ is small is much faster for the unified transform, as noted in § 5.

In this section, errors refer to the difference between the scattered field produced by an array of sound-hard plates and the single plate with boundary condition (2.4), and not to numerical errors (all of the examples below were computed so that numerical errors are negligible compared to physical errors).

7.1 *Near-field*

To quantify the near-field error, we compute the pointwise relative error, $|\tilde{q}(x, y)/q(x, y)|$ for approximations $\tilde{q}$ of q computed using a single plate with various μ (which were listed in § 6.3). The converged reference solution q for an array of sound-hard plates is computed using the unified transform. These errors are shown (in log scale) in Fig. 11 for $k_0 = 0.2$ and Fig. 12 for $k_0 = 2$, both for various values of $2a/d$ and $k_0 d$ (which must be small for the relevant asymptotic regime). We have not shown the errors for larger k_0 since they were very large. As expected, we see large relative errors for the rigid approximation $\mu = 0$. As $2a/d$ and $k_0 d$ decrease, the relative errors away from the plates for μ_0, μ_1 and μ_2 all decrease. There is also an apparent oscillatory shape for the magnitude of the relative errors with height of order d, corresponding to the tips of each plate (hence 4 to 19 wave peaks depending on the parameters). It is also apparent that tapering can, in some cases, reduce the error, but can also sometimes increase the error. These comments underline the importance of edge effects in these types of physical models. It is not clear which choice of tapering is more effective for the smaller $k_0 = 0.2$, but the choice μ_1 is more reliable and effective at reducing the error than μ_2 when $k_0 = 2$.

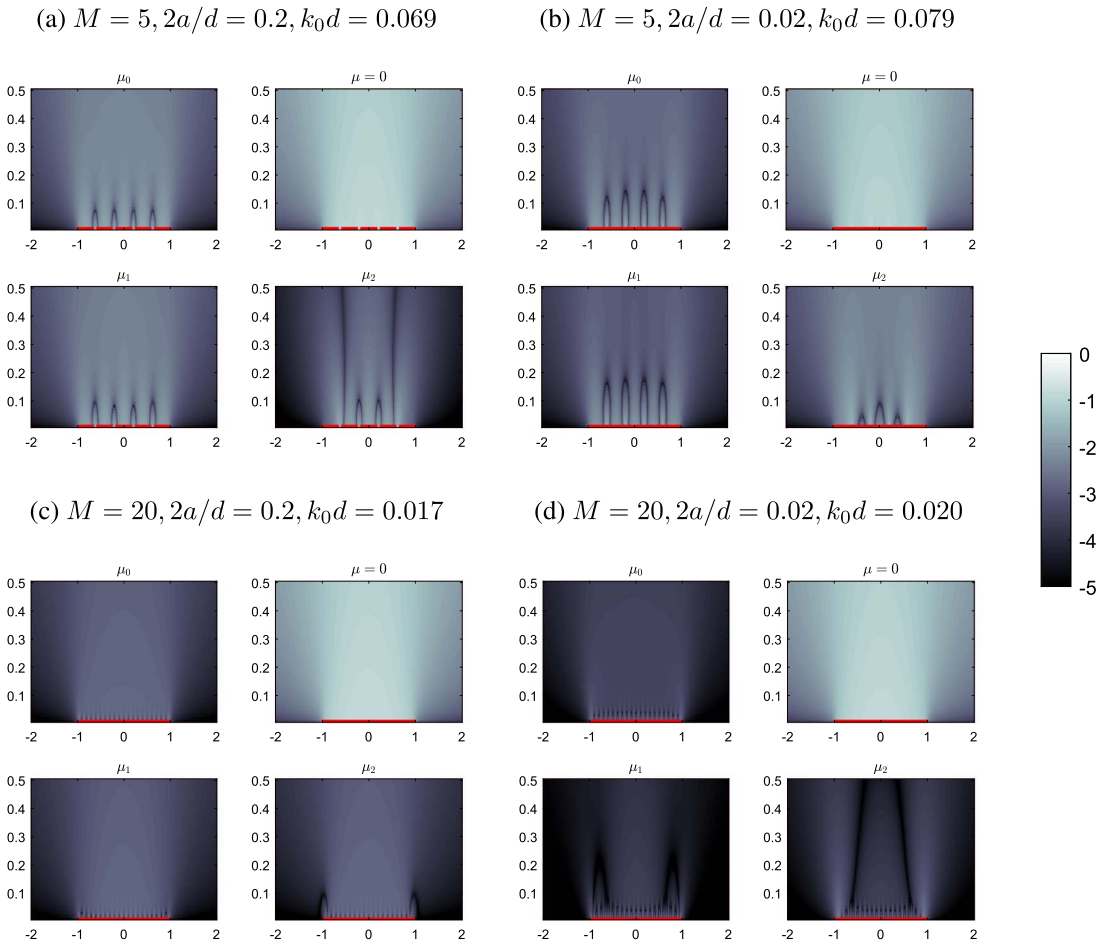

FIG. 11. Near-field relative errors for $k_0 = 0.2$ (screen Helmholtz number = 0.4) shown in `log10` scale. The red lines show the positions of the plates.

7.2 *Far-field*

Figures 13–15 show the relative far-field scattered noise $|D(\theta)|$ for $k_0 = 0.2, 2$ and 10, respectively, with the same parameter selections as before. We have plotted the results for an array of sound-hard plates (computed using the unified transform and iterative Wiener–Hopf method) and denoted by 'True' in the figures. Immediately, we see that when both $2a/d$ and $k_0 d$ are small, there is excellent agreement between the homogenized boundary conditions (with $\mu = \mu_0, \mu_1$ or μ_2) and the sound-hard plates. This agreement verifies the appropriateness of using a constant compliance (neglecting end effects) in this case to provide a good approximation to the physically relevant far-field directivity. However, we see that the number of plates and wavenumber also play important roles. For example, when comparing Fig. 15(d) where there is excellent agreement, to Figs 13(b) and 14(b) where there is less good agreement, despite the open fraction and grating Helmholtz numbers being smaller. This difference again highlights the importance of edge effects—for Fig. 15(d) there are more plates and a

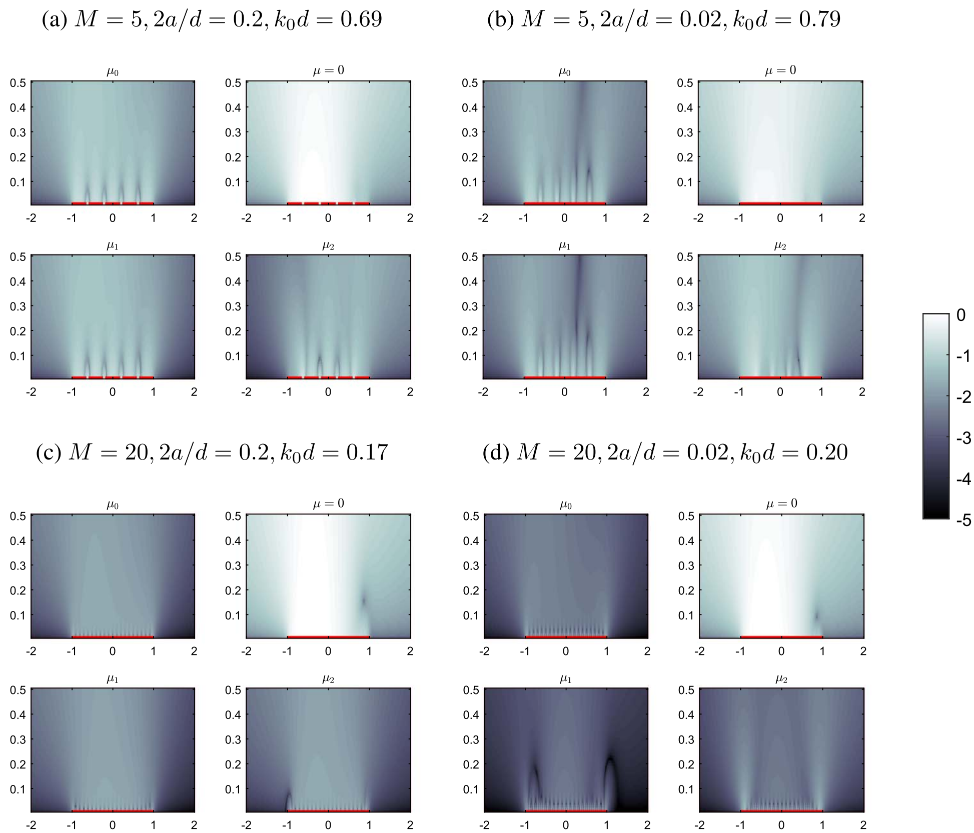

FIG. 12. Near-field relative errors for $k_0 = 2$ (screen Helmholtz number $= 4$) shown in `log10` scale. The red lines show the positions of the plates.

larger wavenumber so edge effects at ± 1 are less important. The different choices also do not seem to affect the number of oscillations in the far-field directivity, even for large wavenumber $k_0 = 10$.

To quantify these results further, we have plotted the relative power (the integral of $|D(\theta)|^2$ divided by the integral corresponding to the array of rigid plates) at infinity for the scattered field for different k_0 in Fig. 16. The left plot shows the relative power as a function of the open fraction for 20 plates. We see that as $2a/d$ decreases, the curves approach 1 for each choice of μ. However, for larger k_0, μ_2 produces an overestimate of the power for small $2a/d$. We see however that if k_0 is small (so that k_0d is small) then μ_2 provides the best estimate for the power. Similarly, in the right plot of Fig. 16, we have plotted the relative power for $2a/d = 0.02$ and various plate numbers M. We see that if M is too small, μ_2 can provide a severe overestimate (which seems to be worse for smaller k_0). For larger k_0, it is also possible for μ_0 and μ_1 to overestimate the power as well. Note also that in all cases, the power produced using μ_2 is greater than when using μ_1, which in turn is greater than μ_0. This highlights the importance of edge effects when considering a finite screen. Moreover, while as we move deeper into the appropriate asymptotic regime (decreasing $2a/d$, k_0d and increasing M), the agreement with the exact case improves. Finally, out of all the physical parameters, it appears that the most important for the homogeneous

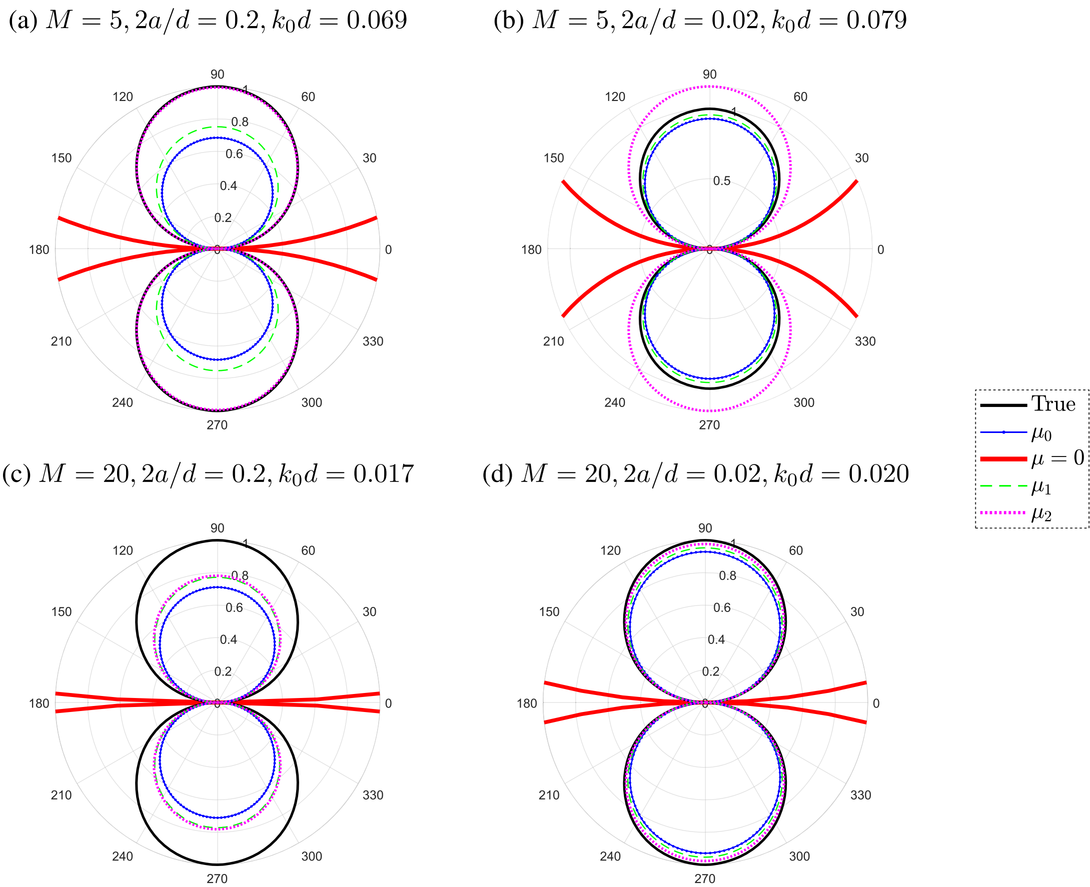

FIG. 13. Relative absolute value of $D(\theta)$ for $k_0 = 0.2$ (screen Helmholtz number = 0.4).

approximation to hold is the open fraction $2a/d$. This is consistent with the homogenization approach in Leppington (1977), which applies the asymptotic limit by considering each gap as a point.

We have also shown the corresponding errors in Fig. 17. These errors highlight the above points—if $2a/d$ and $k_0 d$ are small enough, then μ_2 provides the best estimate of the far field. However, for larger k_0, it can provide a worse estimate than even μ_0 (no tapering). Overall we note that even the simple model of constant compliance can yield good agreement of utility for practical engineering studies, provided there is a sufficiently

- large number of plates, $M > 10$,
- small open fraction $2a/d < 0.04$,
- small grating Helmholtz number $k_0 d < 1$.

However, outside of these limits, one should take care in selecting a compliance parameter for finite sections of perforated materials.

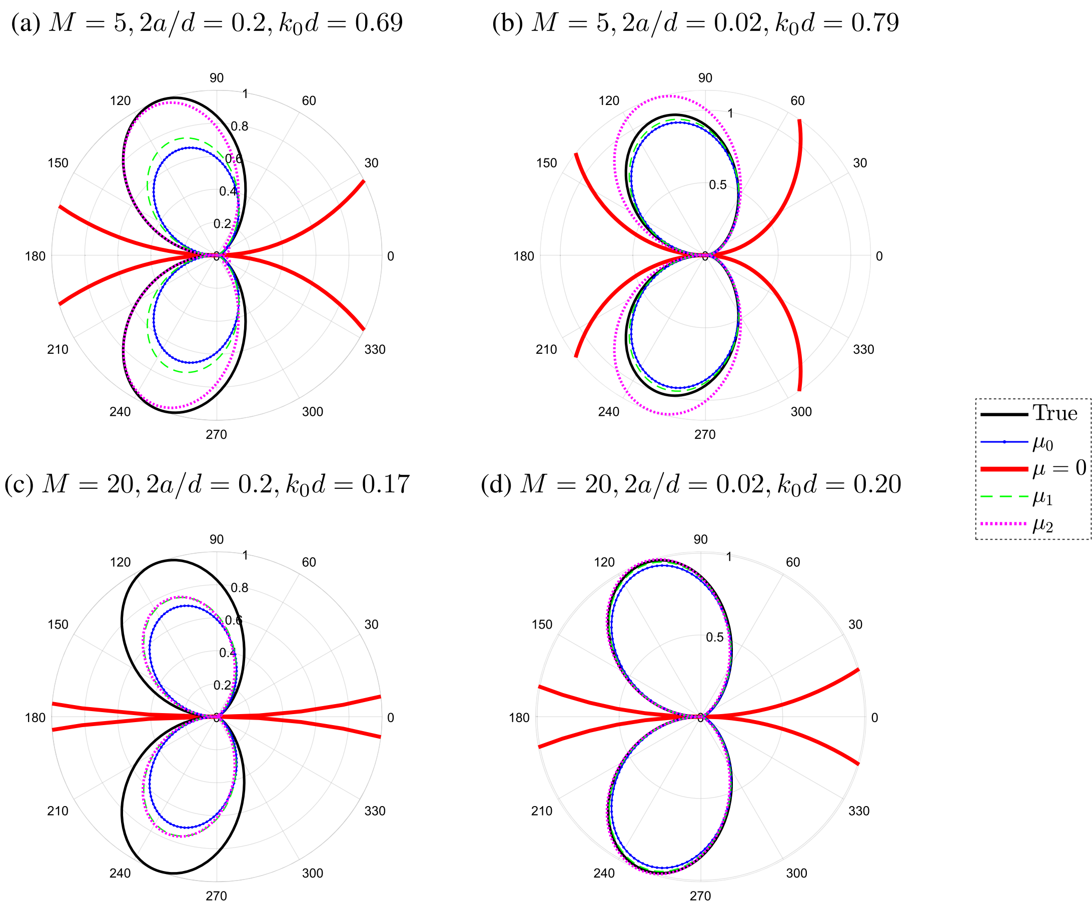

FIG. 14. Relative absolute value of $D(\theta)$ for $k_0 = 2$ (screen Helmholtz number = 4).

8. Conclusion

This paper contributes to understanding the applicability of a compliant or Robin boundary condition to modelling scattering by a truncated array of collinear rigid plates. In particular, we interrogate the role of end effects of such homogenized boundary conditions to finite perforated screens incorporated in larger structures of interest in applications, such as bio-inspired adaptations in aeroacoustics (Kisil & Ayton, 2018). We solve the exact problem using two methods: the unified transform and an iterative Wiener–Hopf method. The former provides a versatile method and is more suited to computing the near field, while the latter is more specialized, most appropriate for large wavenumbers. We detail the regimes in which each method is competitive and practical considerations for implementation, which we hope to be of broader interest to those applying such methods. We found that the unified transform was more appropriate for the asymptotic regimes studied in this paper. This paper also presents an effective collocation approach based on Mathieu functions for tackling the problem of scattering by a finite plate on which a variable Robin boundary condition is applied, which is also likely to be of broader interest.

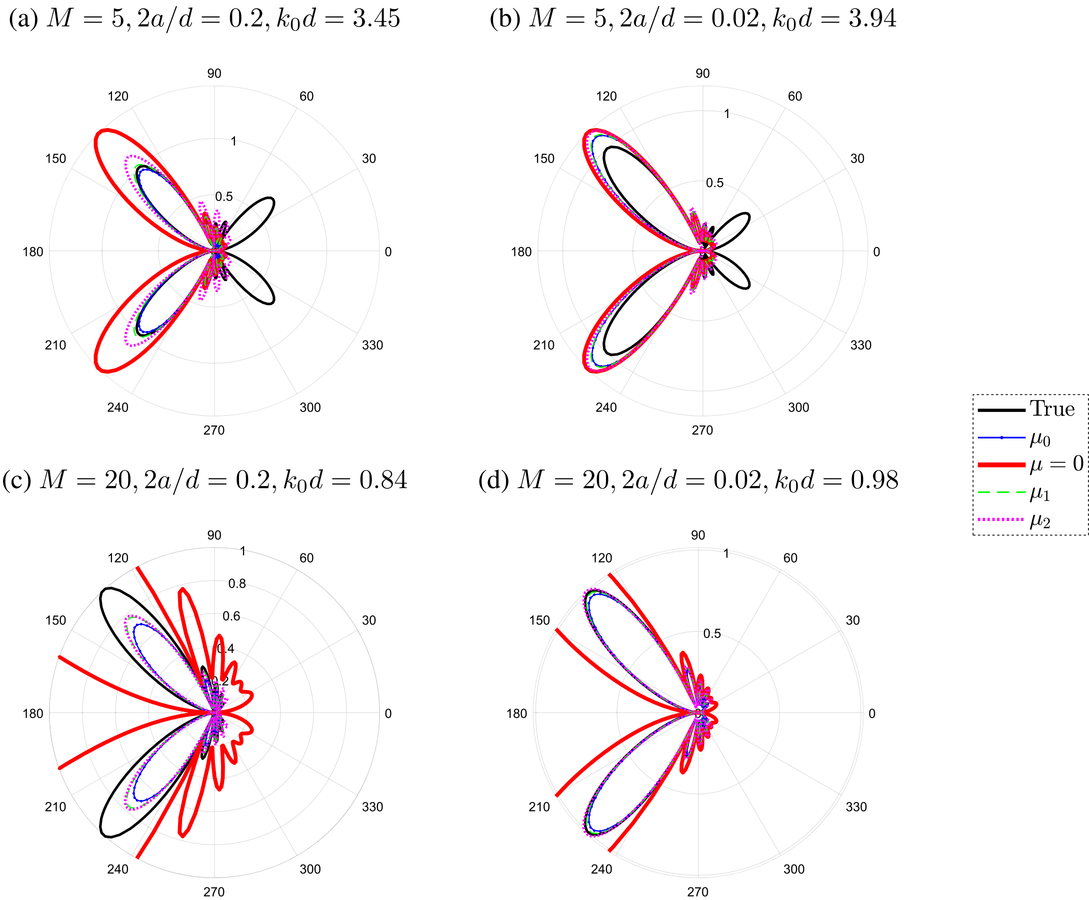

FIG. 15. Relative absolute value of $D(\theta)$ for $k_0 = 10$ (screen Helmholtz number = 20).

We verified the appropriateness of the homogenized constant Robin boundary condition given in Leppington (1977) to achieve good agreement ($< 10\%$) in the far-field directivity with the exact problem even for a modest number of plates (> 10) and sufficiently far into the asymptotic regime of validity for the homogenization ($2a/d < 0.04$) and small k_0. Investigating the role of end corrections to the compliance by taking $\mu \downarrow 0$ to include the sound-hard endpoint junctions can improve the approximation, but a generically suitable manner of tapering is unclear. Nevertheless, a simple tanh-type tapering seemed the most effective choice in this paper for small $2a/d$ and k_0d. These findings, and the slow convergence of the (physical) approximation as we proceed deeper into the appropriate asymptotic regime, highlight the importance of junction effects in scattering problems and may offer an interesting direction for future research should applications require more accurate models. Further, while we anticipate these findings to broadly carry across to alternative homogenization models for structured media, their significance may warrant special interrogation. For each of these points, the extension of the unified transform to variable boundary conditions and the application of the Wiener–Hopf technique

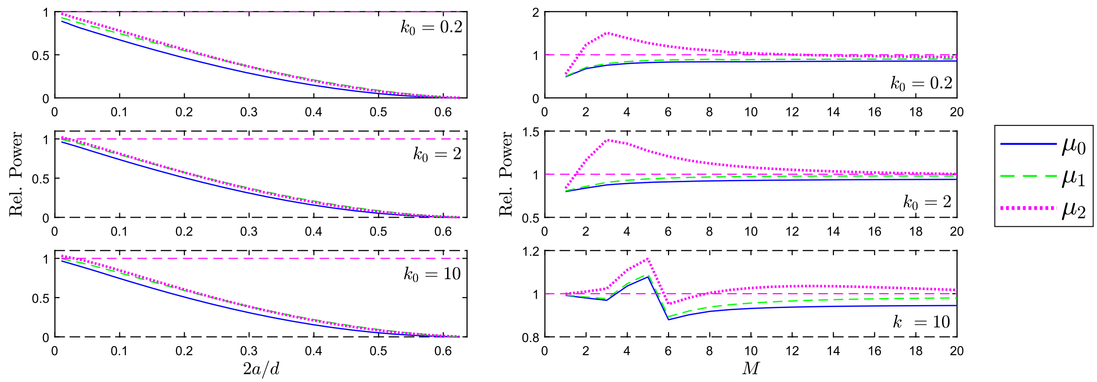

FIG. 16. Relative far-field power for different k_0. Left: For $M = 20$ and various $2a/d$. Right: For $2a/d = 0.02$ and various M.

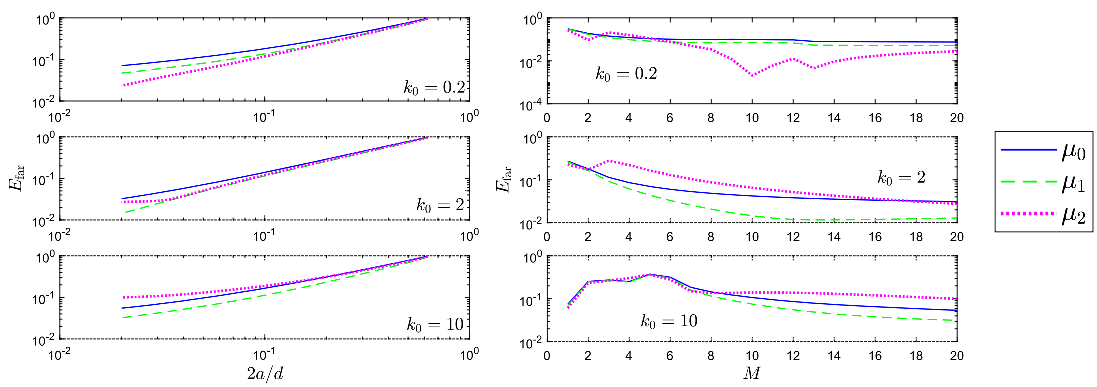

FIG. 17. Same as Fig. 16 but now showing the far-field relative error E_{far}.

to semi-infinite truncated arrays (Capolino & Albani, 2009) may be useful, in addition to the collocation Mathieu function method introduced here for the problem of a finite plate of variable compliance.

Acknowledgements

Example code will also be made available on M.J.C.'s website. M.J.P. and M.J.C. would like to thank Lorna Ayton for discussions and advice during the completion of this work. M.J.C. would like to thank Sonia Flissa, Grégory Vial and John Chapman (who kindly read an initial version) for discussions during the completion of this work.

Funding

Engineering and Physical Sciences Research Council (EP/L016516/1 to M.J.C., EP/N509620/1 to M.J.P.).

References

Achenbach, J. & Li, Z. (1986) Reflection and transmission of scalar waves by a periodic array of screens. *Wave Motion*, **8**, 225–234.

Ayton, L. J., Colbrook, M. J. & Fokas, A. S. (2019) The unified transform: a spectral collocation method for acoustic scattering. *25th AIAA/CEAS Aeroacoustics Conference*, p. 2528 .

Baddoo, P. J., Hajian, R. & Jaworski, J. (2019) A Jacobi spectral collocation method for the steady aerodynamics of porous aerofoils. *AIAA Aviation 2019 Forum* 2959

Boyd, J. (2001) *Chebyshev and Fourier spectral methods*. Courier Corporation .

Camacho, M., Hibbins, A. P., Capolino, F. & Albani, M. (2019) Diffraction by a truncated planar array of dipoles:a Wiener–Hopf approach. *Wave Motion*, **89**, 28–42.

Capolino, F. & Albani, M. (2009) Truncation effects in a semi-infinite periodic array of thin strips: a discrete Wiener–Hopf formulation. *Radio Sci.*, **44**.

Cavalieri, A. V., Wolf, W. R. & Jaworski, J. (2014) Acoustic scattering by finite poroelastic plates. *20th AIAA/CEAS Aeroacoustics Conference*, p. 2459. 00005.

Cavalieri, A. V., Wolf, W. R., and Jaworski, J. (2016) Numerical solution of acoustic scattering by finite perforated elastic plates. *Proc. Royal Soc. A Math. Phys. Eng. Sci.*, **472**, 20150767.

Chen, C.-C. (1971) Diffraction of electromagnetic waves by a conducting screen perforated periodically with holes. *IEEE Trans. Microw. Theory Tech.*, **19**, 475–481.

Colbrook, M. J. (2020) Extending the unified transform: curvilinear polygons and variable coefficient PDEs. *IMA J. Numer. Anal.*, **40**, 976–1004.

Colbrook, M. J. & Ayton, L. J. (2019) A spectral collocation method for acoustic scattering by multiple elastic plates. *J. Sound Vibration*, **461**, 114904.

Colbrook, M. J., Ayton, L. J. & Fokas, A. S. (2019a) The unified transform for mixed boundary condition problems in unbounded domains. *Proc. Royal Soc. A*, **475**, 20180605.

Colbrook, M. J., Flyer, N. & Fornberg, B. (2018) On the Fokas method for the solution of elliptic problems in both convex and non-convex polygonal domains. *J. Comput. Phys.*, **374**, 996–1016.

Colbrook, M. J., Fokas, T. S. & Hashemzadeh, P. (2019b) A hybrid analytical-numerical technique for elliptic PDEs. *SIAM J. Sci. Comput.*, **41**, A1066–A1090.

Colbrook, M. J., Roman, B. & Hansen, A. C. (2019c) How to compute spectra with error control. *Phys. Rev. Lett.*, **122**, 250201.

Dalmont, J. (2001) Acoustic impedance measurement, part I: a review. *J. Sound Vibration*, **243**, 427–439.

Daniele, V., Gilli, M. & Viterbo, E. (1990) Diffraction of a plane wave by a strip grating. *Electromagnetics*, **10**, 245–269.

Erbaş, B. & Abrahams, I. D. (2007) Scattering of sound waves by an infinite grating composed of rigid plates. *Wave Motion*, **44**, 282–303.

Geyer, T., Sarradj, E. & Fritzsche, C. (2010) Measurement of the noise generation at the trailing edge of porous airfoils. *Exp. Fluids*, **48**, 291–308.

Grace, S., Horan, K. & Howe, M. (1998) The influence of shape on the Rayleigh conductivity of a wall aperture in the presence of grazing flow. *J. Fluid. Struct.*, **12**, 335–351.

Grace, S. M., Wood, T. & Howe, M. (1999) Stability of high Reynolds number flow past a circular aperture. *Proc. Royal Soc. London Ser. A Math. Phys. Eng. Sci.*, **455**, 2055–2066.

Graham, R. R. (1934) The silent flight of owls. *Aeronaut. J.*, **38**:837–843. 00124.

Guizal, B. & Felbacq, D. (1999) Electromagnetic beam diffraction by a finite strip grating. *Opt. Commun.*, **165**, 1–6.

Hajian, R. and Jaworski, J. W. (2017) The steady aerodynamics of aerofoils with porosity gradients. *Proc. Royal Soc. A Math. Phys. Eng. Sci.*, **473**, 20170266.

Heins, A. E. & Baldwin, G. L. (1954) On the diffraction of a plane wave by an infinite plane grating. *Math. Scand.*, **2**, 103–118.

Hewett, D. P. and Hewitt, I. J. (2016) Homogenized boundary conditions and resonance effects in Faraday cages. *Proc. Royal Soc. A Math. Phys. Eng. Sci.*, **472**, 20160062.

Howe, M. S. (1998) *Acoustics of Fluid–Structure Interactions*. Cambridge: Cambridge University Press, p. 01080.

Jaworski, J. & Peake, N. (2020) Aeroacoustics of silent owl flight. *Annu. Rev. Fluid Mech.*, **52**.

Jaworski, J. W. & Peake, N. (2013) Aerodynamic noise from a poroelastic edge with implications for the silent flight of owls. *J. Fluid Mech.*, **723**, 456–479.

Jin, Y., Fang, X., Li, Y. & Torrent, D. (2019) Engineered diffraction gratings for acoustic cloaking. *Phys. Rev. Applied*, **11**, 011004.

Kisil, A. & Ayton, L. J. (2018) Aerodynamic noise from rigid trailing edges with finite porous extensions. *J. Fluid Mech.*, **836**, 117–144.

Lamb, H. (1895) *Hydrodynamics*. Cambridge University Press.

Laurens, S., Piot, E., Bendali, A., Fares, M. & Tordeux, S. (2014) Effective conditions for the reflection of an acoustic wave by low-porosity perforated plates. *J. Fluid Mech.*, **743**, 448–480.

Leppington, F. G. (1977) The effective compliance of perforated screens. *Mathematika*, **24**, 199–215.

Lewin, M. & Séré, É. (2010) Spectral pollution and how to avoid it. *Proc. London Math. Soc. (3)*, **100**, 864–900.

Lilley, G. M. (1998). A study of the silent flight of the owl. *CEAS Aeroacoustics Conference*, vol. **2340**, pp. l–6. 00127.

Llewellyn Smith, S. G. & Luca, E. (2019) Numerical solution of scattering problems using a Riemann–Hilbert formulation. *Proceedings of the Royal Society A*. The Royal Society Publishing **475**, 20190105

Martin, C. & Monique, D. (1996) A singularly mixed boundary value problem. *Comm. Partial Differential Equations*, **21**, 1919–1949.

McLachlan, N. W. (1951) *Theory and Application of Mathieu Functions*.

Mghazli, Z. (1992) Regularity of an elliptic problem with mixed Dirichlet–Robin boundary conditions in a polygonal domain. *Calcolo*, **29**, 241–267.

Morse, P. M. & Rubenstein, P. J. (1938) The diffraction of waves by ribbons and by slits. *Phys. Rev. A (3)*, **54**, 895.

Nigro, D. (2017) Prediction of broadband aero and hydrodynamic noise: derivation of analytical models for low frequency. *Ph.D. Thesis*, The University of Manchester (United Kingdom).

Noble, B. (1988) *Methods Based on the Wiener–Hopf Technique for the Solution of Partial Differential Equations*. Chelsea Pub Co.

Nye, J. F. (2002, 2018) Numerical solution for diffraction of an electromagnetic wave by slits in a perfectly conducting screen. *Proc. Royal Soc. London Ser. A Math. Phys. Eng. Sci.*, **458**, 401–427.

Olver, F., Lozier, D., Boisvert, R. & Clark, C. (2010) *NIST Handbook of Mathematical Functions*. Cambridge University Press.

Olver, S. (2011) Computing the Hilbert transform and its inverse. *Math. Comp.*, **80**, 1745–1767.

Otoshi, T. (1971) A study of microwave transmission through perforated flat plates. *Deep Space Netw. Progr. Rep.*, **2**, 80–85.

Priddin, M. J., Kisil, A. V. & Ayton, L. J. (2020) Applying an iterative method numerically to solve n× n matrix Wiener–Hopf equations with exponential factors. *Philos. Trans. Royal Soc. A*, **378**, 20190241.

Priddin, M. J., Paruchuri, C. C., Joseph, P. & Ayton, L. J. (2019) A semi-analytic and experimental study of porous leading edges. *25th AIAA/CEAS Aeroacoustics Conference, p. 2552*.

Rayleigh, L. (1896) *The Theory of Sound*, vol. **2**. Macmillan.

Shanin, A. V. (2003) Diffraction of a plane wave by two ideal strips. *Quart. J. Mech. Appl. Math.*, **56**, 187–215.

Slevinsky, R. M. & Olver, S. (2017) A fast and well-conditioned spectral method for singular integral equations. *J. Comput. Phys.*, **332**, 290–315.

Spence, E. (2011) Boundary value problems for linear elliptic PDEs. *Ph.D. Thesis*, University of Cambridge.

Sturman, B., Podivilov, E. & Gorkunov, M. (2011) Optical properties of periodic arrays of subwavelength slits in a perfect metal. *Phys. Rev. B*, **84**, 205439.

Trogdon, T. & Olver, S. (2016) *Riemann–Hilbert Problems, Their Numerical Solution, and the Computation of Nonlinear Special Functions*. SIAM.